1 **TITLE PAGE**

2 **A gated hydrophobic funnel within BAX binds long-chain alkenals to potentiate pro-**
3 **apoptotic function**

4 Jesse D. Gelles[1,2,3], Yiyang Chen[1,2,3,4], Mark P. A. Luna-Vargas[1,2,3], Ariele Viacava Follis[5], Stella
5 G. Bayiokos[1,2,3,4], Jarvier N. Mohammed[1,2,3], Tara M. Sebastian[1,2,3], M. Abdullah Al Noman[1,2,3],
6 Ngoc Dung Pham[6], Yi Shi[6], Richard W. Kriwacki[5,7], and Jerry E. Chipuk[1,2,3,4,8,9]*

7 [1] Laboratory of Mitochondrial Biology in Human Health and Disease, Icahn School of Medicine at
8 Mount Sinai, One Gustave L. Levy Place, New York, New York 10029, USA
9 [2] Department of Oncological Sciences, Icahn School of Medicine at Mount Sinai, One Gustave L.
10 Levy Place, New York, New York 10029, USA
11 [3] The Tisch Cancer Institute, Icahn School of Medicine at Mount Sinai, One Gustave L. Levy Place,
12 New York, New York 10029, USA
13 [4] The Graduate School of Biomedical Sciences, Icahn School of Medicine at Mount Sinai, One
14 Gustave L. Levy Place, New York, New York 10029, USA
15 [5] Department of Structural Biology, St. Jude Children's Research Hospital, 262 Danny Thomas
16 Place, Memphis, Tennessee 38105, USA
17 [6] Department of Pharmacological Sciences, Icahn School of Medicine at Mount Sinai, One
18 Gustave L. Levy Place, New York, New York 10029, USA
19 [7] Department of Microbiology, Immunology and Biochemistry, University of Tennessee Health
20 Sciences Center, Memphis, Tennessee 38105, USA
21 [8] Department of Dermatology, Icahn School of Medicine at Mount Sinai, One Gustave L. Levy
22 Place, New York, New York 10029, USA
23 [9] The Diabetes, Obesity, and Metabolism Institute, Icahn School of Medicine at Mount Sinai, One
24 Gustave L. Levy Place, New York, New York 10029, USA
25 * Correspondence: jerry.chipuk@mssm.edu

ABSTRACT

Mitochondria maintain a biochemical environment that cooperates with BH3-only proteins (e.g., BIM) to potentiate BAX activation, the key event to initiate physiological and pharmacological forms of apoptosis. The sphingosine-1-phosphate metabolite 2-trans-hexadecenal (2t-hexadecenal) is one such component described to support BAX activation, but molecular mechanisms remain largely unknown. Here, we utilize complementary biochemical and biophysical techniques to reveal that 2t-hexadecenal non-covalently interacts with BAX, and cooperates with BIM to stimulate early-activation steps of monomeric BAX. Integrated structural and computational approaches reveal 2t-hexadecenal binds an undefined region – a hydrophobic cavity formed by core-facing residues of α5, α6, and gated by α8 – we now term the "BAX actuating funnel" (BAF). We define alkenal length and α8 mobility as critical determinants for 2t-hexadecenal synergy with BIM and BAX, and demonstrate that proline 168 allosterically regulates BAF function. Collectively, this work imparts detailed molecular insights advancing our fundamental knowledge of BAX regulation and identifies a regulatory region with implications for biological and therapeutic opportunities.

KEYWORDS

49 **INTRODUCTION**

50 Developmental, homeostatic, and pharmacological pro-apoptotic signals converge by engaging
51 the BCL-2 family of proteins to induce BAX-dependent mitochondrial outer membrane
52 permeabilization (MOMP) and apoptosis.[1] Despite sequence and structural similarity with multiple
53 globular BCL-2 family proteins, BAX is unique in that it converts from an inactive cytosolic
54 monomer to pore-forming oligomer at the outer mitochondrial membrane (OMM). Upon transient
55 triggering with direct activator BH3-only proteins (e.g., BIM, BID), BAX undergoes a series of
56 intramolecular rearrangements and structural refoldings that ultimately result in translocation to
57 the OMM, oligomerization, and MOMP.[2-7] An important structural event during this process is α9
58 helix mobilization from its residence within the BAX BC groove, which simultaneously supports
59 OMM translocation, BAX:BAX interactions, and propagation of the activation process leading to
60 proteolipid pore formation. We refer to this series of structural rearrangements as the BAX
61 activation continuum, which may be separated into an activation phase (triggering) and
62 functionalization phase (pore formation).[8]

63 There are two general requirements for potent BAX activation: protein-protein interactions to
64 trigger the monomer, and protein-lipid interactions to initiate and stabilize refolding of BAX into
65 multimeric conformers. These requirements are proposed to occur in distinct phases of the
66 activation continuum, and most insights into protein-lipid interactions focus on how BAX interacts
67 within the OMM to form pore-like structures.[9-12] This has led to a modern conceptualization in
68 which mitochondrial membranes actively cooperate with the BCL-2 family to control cell death
69 commitment.[13] Notably, mitochondrial endoplasmic reticulum contact sites (MERCS) maintain
70 lipid homeostasis between the organelles and supply lipids that are critical for MOMP.[14] One
71 example, the terminal end-product of the sphingolipid pathway – 2-trans-hexadecenal
72 (2t-hexadecenal) – is required for BAX-mediated MOMP following triggering by BIM or BID.[15]
73 2t-hexadecenal is formed by the irreversible cleavage of sphingosine-1-phosphate (S1P) and is
74 metabolized to palmitoyl-CoA for fatty acid synthesis pathways.[16] The resident enzymes
75 responsible for generating and catabolizing 2t-hexadecenal are enriched at MERCS, and
76 genetically modulating 2t-hexadecenal levels alters sensitivity to human BAX in yeast.[17]
77 Additionally, interactions between BAX and the OMM are governed by OMM curvature, which is
78 regulated by a combination of the mitochondrial dynamics machinery, intra-organellar membrane
79 contact sites, and mitochondria-specific lipids.[18,19]

80 While the requirement for 2t-hexadecenal in the BAX activation continuum is described,
81 cooperation with BH3-only proteins and underlying mechanisms remain poorly understood. Here,
82 we utilize biochemical, biophysical, structural, and computational approaches to systematically
83 demonstrate that 2t-hexadecenal directly actuates BAX through non-covalent interactions at a
84 previously undefined region – a funnel-shaped hydrophobic cavity formed by core-facing residues
85 of α5, α6, and gated by α8, which we term the BAX Actuating Funnel, or BAF. Our results suggest
86 that BIM-mediated BAX triggering mobilizes α8, making the BAF accessible, and that binding of
87 2t-hexadecenal promotes BAX functionalization. Furthermore, we identify chemical and structural
88 determinants underlying the 2t-hexadecenal:BAX interaction and reveal that mutation of proline
89 168 in the loop between α8 and α9 allosterically deforms the BAF and subsequently disrupts the
90 function of 2t-hexadecenal. Collectively, this model advances our understanding of the BAX
91 structure-function relationship by characterizing the protein-lipid interactions responsible for
92 stimulating monomeric BAX activation and identifies a previously underappreciated regulatory
93 domain for both cell biology and therapeutic investigations.

94 **RESULTS**

95 **2t-hexadecenal directly activates BAX through non-covalent interactions**

96 Previous work demonstrated that hexadecenal was required for potent BAX-mediated MOMP and
97 that sphingolipid precursors are supplied to mitochondria via interactions with heterotypic
98 membranes.[15] To assess whether ectopic hexadecenal exposure could engage BAX activation *in*
99 *cellulo*, we treated SV40-transformed mouse embryonic fibroblasts (MEFs) with increasing
100 concentrations of hexadecenal and measured the apoptotic response using our real-time multi-
101 visitation microscopy technique, SPARKL.[20] Supraphysiological concentrations of ectopic
102 hexadecenal ("2t-16") did not induce cell death at the lower concentrations tested (Figure 1A).
103 We reasoned that any pro-apoptotic signaling may have been mitigated by the repertoire of anti-
104 apoptotic BCL-2 family proteins, and indeed, co-treatment with the BH3-mimetic ABT-737
105 revealed an apoptotic phenotype in response to ectopic hexadecenal (Figure 1A). To determine
106 if the apoptotic response required triggering by direct activators, we utilized *Bim*$^{-/-}$*Bid*$^{-/-}$ double
107 knockout (DKO) MEFs and observed a loss of apoptosis at lower concentrations of ectopic
108 hexadecenal co-treated with ABT-737, suggesting that BAX activation was part of the underlying
109 mechanism (Figure 1B). Finally, we replicated this experiment in *Bax*$^{-/-}$*Bak*$^{-/-}$ DKO MEFs and
110 observed no cell death (Figure 1C). Collectively, these data support the conclusion that
111 hexadecenal induces apoptotic cell death by acting on effector BCL-2 family proteins.

112 There are reports that ectopic hexadecenal can form adducts with DNA and generate oxidative
113 stress resulting in apoptosis[21,22]; therefore, we interrogated whether hexadecenal directly
114 promoted BAX-mediated pore formation by utilizing recombinant BAX protein and large
115 unilamellar vesicles (LUVs), which are biochemically-defined liposomes that mimic the major lipid
116 composition of the OMM, and assessed BAX activation by measuring LUV permeabilization.
117 While recent studies have incorporated hexadecenal directly into the formulation of LUVs[23], we
118 aimed to investigate hexadecenal-mediated BAX activation without altering the biochemistry of
119 the LUV membrane. BAX treated with supraphysiological concentrations of hexadecenal
120 demonstrated dose-dependent activation and LUV permeabilization (Figure 1D). Importantly,
121 ectopic hexadecenal alone did not disrupt or cause leakage of LUVs (Figure S1B). In the cell,
122 BAX activation is mediated primarily through BCL-2 family direct activators – predominantly, BIM[24]
123 – and we had observed inhibited apoptosis in the *Bim*$^{-/-}$*Bid*$^{-/-}$ MEFs; therefore we sought to
124 assess the cooperation of BIM and hexadecenal on BAX-mediated membrane permeabilization.
125 We treated BAX with an activating concentration of BIM-BH3 peptide and observed a dose-
126 dependent increase and acceleration in LUV permeabilization in response to hexadecenal
127 (Figures 1E, S1A). Furthermore, the synergy with hexadecenal was observed with mildly-
128 activating concentrations of BIM-BH3 as well (Figures 1F, S1C). Previous work indicated that the
129 saturated form of 2t-hexadecenal – hexadecanal ("16CHO") – did not induce BAX oligomers in
130 cross-linking studies[15], and indeed, we did not observe BAX-mediated pore formation or synergy
131 with BIM in response to hexadecanal (Figures 1G–I, S1D). These data indicate that hexadecenal
132 promotes BAX pore formation and synergizes with BIM activation.

133 Despite treating BAX with hexadecenal directly, we could not entirely rule out the possibility that
134 increased permeabilization could have been due to the lipidic aldehyde interacting with LUVs and
135 resulting in a more permissive environment for BAX pore formation. Therefore, we utilized
136 microscale thermophoresis (MST) to determine whether hexadecenal directly bound to BAX and
137 observed a dose-dependent shift indicating changes to the molecular volume of BAX in response

138   to hexadecenal (Figure 2A). Interestingly, the saturated hexadecanal aldehyde did not induce a
139   similar change in BAX thermophoresis, suggesting that the α,β double bond is necessary for BAX
140   interaction and subsequent activation (Figures 2B, S2A).

141   Hexadecenal is an α,β-unsaturated aldehyde and is capable of modifying nucleophiles, (e.g.,
142   cysteine residues) through Michael addition, and the requirement for the double bond suggested
143   a chemical reaction mechanism.[25] In fact, recent publications have reported that hexadecenal
144   covalently modifies BAX, though the studies disagree on which cysteine residue is modified and
145   it is unclear whether the reaction is biologically specific to BAX.[23,26] To determine whether the
146   mechanism of hexadecenal-mediated BAX activation was the result of covalent modification, we
147   incubated BAX with hexadecenal and subjected the sample to higher-energy collision-induced
148   dissociation (HCD) and tandem liquid chromatography-mass spectrometry (LC-MS). We detected
149   peptide fragments covering both cysteines (C62, C126) and observed no alkylation by
150   hexadecenal (m+238.229 Da); as a control, we were able to detect modification of the cysteines
151   by the alkylating agent iodoacetamide (m+57.021 Da) (Figure 2C). Additionally, we also observed
152   no shift by intact mass spectrometry (data not shown). To decisively conclude that the mechanism
153   was independent of cysteine modification, we replicated our LUV permeabilization studies using
154   a cysteine-replacement BAX mutant (BAX[C62S,C126S], "BAX[2S]"), which exhibited no changes to
155   stability or melting temperature (Figure S2B). Compared to wild-type BAX ("BAX[WT]"), BAX[2S]
156   remained sensitive to hexadecenal-mediated changes in melting temperature, pore formation,
157   and synergy with BIM-BH3 peptide (Figures 1D–F, 2D–F, S2C–D). Additionally, BAX[2S] remained
158   similarly unaffected by the saturated hexadecanal aldehyde (Figures 2G–I, S2E). Collectively,
159   these results indicate that hexadecenal promotes BAX pore formation through a direct, non-
160   covalent interaction mechanism.

161   **2t-hexadecenal synergizes with BIM and promotes early-activation steps of monomeric**
162   **BAX**

163   The BAX activation continuum can be divided into two distinct phases of activation and
164   functionalization: the cytosolic monomer gets activated and undergoes intramolecular
165   rearrangements and conformational changes that result in translocation to the OMM;
166   subsequently, active BAX proteins in the OMM undergo large-scale conformational changes,
167   oligomerize, and mature into pore-forming units. Our data thus far measured BAX
168   functionalization (i.e., pore formation) and demonstrated that hexadecenal cooperates with BIM
169   to promote membrane permeabilization. Previous studies demonstrating hexadecenal-mediated
170   BAX activation were mostly limited to model membranes with endogenous or incorporated
171   hexadecenal, often at supraphysiological concentrations.[15,23] In contrast, we utilized a direct
172   treatment model of hexadecenal and BAX protein, indicating that the mechanism of action likely
173   occurs on BAX found in the cytosol and prior to integration within the OMM. To investigate the
174   effect of hexadecenal specifically on the activation phase of BAX, we utilized a technique we
175   developed called FLAMBE, which monitors activation-induced intramolecular rearrangements
176   within BAX (i.e., rearrangements that result in early-activation structural hallmarks such as
177   displacement of the α1–α2 loop and mobilization of the C-terminal α9 helix).[4,8] FLAMBE observes
178   real-time early-activation of BAX by measuring changes in Polarization resulting from the kinetic
179   binding and dissociation of a TAMRA-labeled BAK-BH3 peptide (BAK[TAMRA]); broadly, BAX
180   activation can be inferred by measuring a reduction of Polarization over time (Figure S3A). Kinetic
181   FLAMBE data can further be parameterized into time-of-maximum-Polarization (Tmax) and
182   endpoint Polarization (EP) for trend overviews and comparative analyses between treatment

183 conditions (Figures S3B). As an example, BAX treated with a range of BIM concentrations exhibits
184 a dose-dependent pattern of BAK^{TAMRA} dissociation (measured as a reduction in Polarization over
185 time) indicative of BAX activation (Figure S3C).

186 Using FLAMBE, we observed BAX^{WT} activation in the presence of hexadecenal as demonstrated
187 by a reduction in Polarization over time, indicating that high concentrations of hexadecenal could
188 induce a "direct-activator"-like effect on BAX monomers (Figure 3A). To confirm that this
189 phenotype was not due to covalent modification of cysteine residues, we replicated the FLAMBE
190 experiment with BAX^{2S} and observed the same activation profile (Figure 3B). By contrast, neither
191 BAX^{WT} nor BAX^{2S} activated in response to the saturated hexadecanal aldehyde, though we did
192 observe some destabilization of the BAX:BAK^{TAMRA} heterodimer at the higher concentrations
193 (Figure S3D–E). We hypothesized that hexadecenal cooperates with direct activators instead of
194 activating BAX *de novo* within the cell, and thus we investigated whether the synergy between
195 hexadecenal and BIM occurs during the early-activation phase. We treated BAX^{2S} with a non-
196 activating concentration of BIM-BH3 to generate a population of stable BIM:BAX:BAK^{TAMRA}
197 heterotrimers (Figure 3C, yellow data). The addition of a non-activating concentration of
198 hexadecenal resulted in activation of the primed BAX^{2S} population (Figure 3C, left panel);
199 moreover, activation of primed BAX^{2S} was observed with several non-activating concentrations of
200 hexadecenal (Figure 3C, right panel). When we induced a "triggered" BAX population (i.e., mildly
201 activated by BIM), we similarly observed increased activation by non-activating concentrations of
202 hexadecenal, as measured by increased kinetics of BAK^{TAMRA} dissociation, greater shifts in
203 parameterized metrics, and reduction in area under the curve (Figures 3D, S3F). Importantly, we
204 observed the same outcomes with BAX^{WT}, confirming that the mechanism was not due to the
205 endogenous cysteines or their mutation (Figure S3G). To eliminate the possibility that
206 hexadecenal was inducing BAK^{TAMRA} dissociation by competing for the BC groove, we treated
207 recombinant BCL-xL in the presence of BAK^{TAMRA} and observed no competition by hexadecenal
208 (Figure S3H).

209 The consequence of BAX activation is translocation to the OMM and oligomerization, and while it
210 is largely agreed that high-molecular weight oligomers are formed within the OMM, there is
211 evidence supporting that physiologically-activated BAX forms low-order multimers (e.g., dimers)
212 in solution prior to integrating with membranes.[6,8,27] We investigated the consequence of
213 hexadecenal-mediated synergy with BIM-activated BAX by performing size exclusion
214 chromatography (SEC) and observed a substantial shift from monomeric to dimeric BAX when
215 co-treated with BIM-BH3 peptide and hexadecenal (Figure 3E). To confirm that the earlier peak
216 was BAX, we treated fluorescently-labeled BAX, subjected it to SEC, and screened the fractions
217 for fluorescence. The monomeric BAX peak (fractions 28–31) shifted slightly left upon addition of
218 hexadecenal or BIM-BH3 peptide (fractions 27–30), likely due to binding-dependent changes in
219 molecular volume, and dimeric species were observed in the BIM-treated sample (fractions 23–
220 26); the co-treatment of hexadecenal and BIM-BH3 resulted in an increased shift and intensity
221 indicating a greater percent of the BAX population formed multimeric species (fractions 22–26)
222 (Figure 3F). By contrast, no such shift in the monomeric peak or BIM-induced dimer peak was
223 observed with hexadecanal (Figure 3G). Of note, BAX activated in solution does not readily form
224 high-molecular weight species without the stabilizing and concentrating influence of a
225 hydrophobic environment (e.g., a membrane or micellar detergent)[8,28], though as a reference we
226 were able to observe BAX oligomers generated with a detergent (BAX$_O$).[29] These data collectively
227 demonstrate that hexadecenal promotes monomeric BAX activation downstream of BCL-2 protein
228 interactions and following activation by direct activators.

An alpha 8 helix-gated funnel-shaped hydrophobic cavity in the BAX core interacts with 2t-hexadecenal

Hexadecenal synergized with BIM-mediated BAX activation and we observed no evidence of competition with the BAK[TAMRA] peptide in our FLAMBE assays, suggesting that hexadecenal was binding to a site distinct from either the trigger site or BC groove, the two BH3-interacting sites respectively.[30,31] Despite having a relatively smooth surface and no obvious "binding pocket," studies have identified small molecules that bind to BAX, either at BH3-interacting sites or allosterically.[32-34] To identify putative interaction sites, we performed 2D ^{1}H-^{15}N heteronuclear single quantum coherence (HSQC) nuclear magnetic resonance (NMR) of ^{15}N-labeled BAX[WT] treated with hexadecenal and measured a multitude of peak shifts (Figures S4A−B). Several residues exhibited significant chemical shift perturbations (CSPs) in response to hexadecenal, some of which were within unstructured regions (such as the N-terminus) or highly exposed areas (such as α4 and α9), but notably the two cysteine residues (C62 and C126) did not reach significance (Figure 4A). Interestingly, several shifts were observed in core-facing residues of α2, α5, α6, and α8, as well as bulky residues proximal to α8 within the α4–5 loop and α7. To determine whether the shifted residues were specific to the activation mechanism, we compared this CSP profile against CSPs calculated from ^{1}H-^{15}N HSQC NMR of BAX[WT] treated with the non-activating saturated aldehyde. Residues exhibiting significant shifts in response to hexadecanal were more localized to accessible regions of BAX along α2, α3, and α9 (Figure S4C). Comparing the CSPs of the two aldehydes highlighted that many of the hexadecenal-induced shifts were not observed with the saturated aldehyde (Figure S4D). These core-facing residues are not believed to be readily accessible and therefore were likely to be meaningful for hexadecenal interaction and function.

Inspection of the BAX structure revealed a cavity formed by hydrophobic residues in the core of the protein.[6] The cavity shape resembles a funnel and is comprised of two topographies: a wide and shallow "mouth" formed by residues in α1, α2, α5, and α8; a narrow "neck" extending into the BAX core between α1, α5, and α6 (Figure 4B). We hypothesized that this hydrophobic "funnel" could be a desirable interaction site for hexadecenal – an inherently lipidic aldehyde – and therefore we performed unbiased *in silico* docking simulations using the SwissDock web service to model interactions with BAX. Binding modalities of hexadecenal were clustered into a few distinct regions on BAX, but 59.4% of the poses were proximal to α8, aligning with the CSPs observed by NMR (Figure 4C).

Our functional interrogations indicated that hexadecenal synergizes with BIM-mediated BAX activation, and we reasoned that BIM-induced intramolecular arrangements may induce flexibility and/or mobility of α8, making the funnel accessible to hexadecenal. SwissDock utilizes rigid receptor docking, which results in the α8 helix firmly blocking the funnel. To create a funnel-accessible structure, we removed α8 (BAX[Δα8]) and docking against the BAX[Δα8] structure revealed a clear preference for the funnel with 97.3% of hexadecenal poses positioned within the funnel (Figure 4D). Interestingly, when we examined the solution NMR structure of BAX bound to a stapled BIM-BH3[30], we observed an enlargement of the hydrophobic funnel, most notably in the neck of the funnel (Figure 4E). In the unbound BAX structure, the neck of the funnel is cinched into discontinuous cavities by residues of α5 and α6; in contrast, the BIM-bound structure has a connected cavity due to a shift in the residues lining the funnel, increasing both the depth and width. Docking hexadecenal against the BAX:BIM structure with α8 removed (BAX[Δα8]:BIM) revealed that the aldehyde was positioned in the funnel, frequently posed as being inserted into the neck of the funnel (Figure 4F).

275   To substantiate our *in silico* conclusions, we engineered a structural mutant of BAX to restrict the
276   mobility of α8 and the subsequent access to the hydrophobic funnel. We introduced two cysteine
277   residues into BAX[2S] (L59C, C62S, C126S, L162C; "BAX[α8]") that could be oxidized to induce a
278   disulfide tether between α2 and α8 (Figure 4G). We characterized the consequence of the new
279   mutations by activating BAX[α8] with BIM-BH3 peptide and assessing LUV permeabilization.
280   Reduced BAX[α8] (i.e., "unlocked") remained functional and exhibited BIM-induced LUV
281   permeabilization (Figure S4E); in contrast, oxidized BAX[α8] (i.e., "locked") demonstrated no
282   permeabilization (Figure S4F). Several studies have characterized that BAX functionalization and
283   pore formation required large-scale conformational reorganization, which involves the separation
284   of α8 from core helices, and therefore it is not surprising that BAX[α8] was a "functionally dead"
285   structural mutant.[5-7,35] However, we recently demonstrated that several historically "dead" BAX
286   mutants remain sensitive to BH3-induced activation and demonstrate early-activation structural
287   hallmarks despite not maturing into functional pore-forming conformations.[8] SEC experiments
288   revealed that locked BAX[α8] exhibited a shift in response to BIM-BH3 but was unaffected by either
289   hexadecenal alone or coupled with BIM-mediated activation (Figure 4H). To further investigate
290   whether the immobilized α8 helix would disrupt sensitivity to hexadecenal, we studied BAX[α8]
291   activation using our FLAMBE assay. Both the unlocked and locked forms of BAX[α8] demonstrated
292   activation by BIM-BH3, indicating that that the mutant still exhibits activation-induced
293   intramolecular rearrangements (Figures S4G–H). Critically, locked BAX[α8] did not activate when
294   treated with hexadecenal (Figure S4I). Moreover, BIM-primed BAX[α8] displayed no activation or
295   synergy in the presence of hexadecenal (Figures 4I, S4J). These data substantiate the docking
296   simulations and the conclusion that hexadecenal-induced BAX activation is mediated through
297   non-covalent interactions with the hydrophobic funnel in the BAX core, which is exposed following
298   BIM triggering. Given that this hydrophobic cavity potentiates BAX activation, we termed this site
299   the "BAX Actuating Funnel", or BAF.

Aldehyde length and BAF topography are determinants of BAX activation

301   The saturated aldehyde hexadecanal did not activate BAX suggesting that the mechanism is
302   unique to 2t-hexadecenal. We next considered the relevance of aldehyde length on interactions
303   with the BAF by utilizing a panel of 2t-alkenals ranging from 5 to 13 carbon chains (henceforth,
304   "alkenals"). Experiments with a mid- or short-chain alkenal, nonenal ("2t-9") and pentenal ("2t-5"),
305   respectively, demonstrated CSP profiles that were similar to hexadecenal, but were also more
306   diffuse across BAX (Figure 5A). While there was some conservation of CSPs observed in
307   residues within and proximal to α8, the shorter alkenals exhibited a plethora of shifts within α4
308   and α9 as well as a general trend of interacting with solvent-exposed residues (Figure S5A).
309   These data may also indicate that shorter alkenals are more promiscuous, as nonenal and
310   especially pentenal interacted with several accessible regions of BAX, exhibited decreasing
311   specificity at higher concentrations, and displayed weaker CSPs (Figures S5B–C). Docking
312   simulations with alkenals ranging from 5 to 15 carbon chains supported this hypothesis by
313   demonstrating a length-dependent specificity for the α8 region (in the full-length structure, BAX)
314   or the BAF (in the BAX[Δα8] structure) (Figures 5B, S6A–B). When docked against the BAX[Δα8]:BIM
315   structure, most alkenal species were predicted to interact with the larger BAF, though many were
316   not positioned in the depth of the funnel and short-chain aldehydes could not occupy both the
317   mouth and neck of the BAF in the same pose (Figure S6C). In the BIM-bound BAX structure,
318   mobilization of the α1–α2 loop created a region that was predicted to be an interaction site, and
319   longer aldehyde structures were disproportionately positioned as a consequence; we believe this
320   was an artifact of rigid receptor docking and not a physiological phenomenon, and therefore we

321 did not quantify the percentage of binding poses localized to the BAF. The precursor of
322 2t-hexadecenal, sphingosine 1-phosphate (S1P), was previously identified as a requirement for
323 BAK-mediated MOMP but did not directly promote BAX-mediated MOMP.[15] We docked the
324 structure of S1P against BAX models and observed a reduced preference for the BAF and the tail
325 could not occupy the neck of the BAF when modeled against BAX$^{\Delta\alpha8}$:BIM structure, likely due to
326 the bulky and negatively charged phosphate group (Figures 5B, S6A–C). Collectively, NMR and
327 unbiased docking assessments supported our hypothesis that aldehyde length promotes
328 specificity for the BAF and BAX activation.

329 Next, we tested our hypothesis by investigating which, if any, alkenals could phenocopy
330 hexadecenal function and BAX activation. When subjected to MST, BAX^{WT} exhibited altered
331 thermophoresis with each of the alkenals; though the fit of the data demonstrated a trend in which
332 the slope increased with aldehyde length (Figures 5B, S7A). To interrogate the functional
333 consequence of alkenals interacting with BAX, we next subjected each alkenal to FLAMBE
334 analysis and observed a dependency on aldehyde length for BAX^{2S} activation (Figure 5D).
335 Interestingly, at the concentrations we tested, undecenal ("2t-11") and dodecenal ("2t-12")
336 displayed some disruption of BAX^{2S}:BAK^{TAMRA} interactions, similar to the results with hexadecanal,
337 but BAK^{TAMRA} was able to re-bind and did not exhibit an activation profile (Figures S3E, S7B).
338 When compared to hexadecenal, only tridecenal ("2t-13") exhibited a clear dose-dependent
339 activation trend, albeit less potently than hexadecenal (Figures 5D–E, S7B). To definitively
340 determine alkenal-induced BAX activation, we performed LUV permeabilization studies and
341 confirmed a length-dependent sensitivity for BAX^{2S}-mediated pore formation (Figures 5F, S7C).
342 Additionally, these results were conserved in experiments using BAX^{WT} (data not shown). Taken
343 together with our structural and modeling data, these results indicate that chain length is a
344 determinant of α,β-unsaturated alkenals to specifically target the BAF and activate.

345 Having identified determinants of ligand specificity, we next sought to characterize the residues
346 of the BAF that regulate interactions with, and sensitivity to, hexadecenal. We performed
347 molecular docking of hexadecenal against the BAX:BIM structure using the GLIDE software with
348 a docking grid centered on the BAF. As we expected, the residues lining the BAF that interact
349 with hexadecenal were predominantly hydrophobic residues of α5 and α6 and all predicted poses
350 were positioned into the neck of the BAF (Figures 6A−B). We performed a virtual mutagenesis
351 screen using the BAX structure and identified that mutating V110, L113, or L144 to bulkier
352 residues was predicted to alter the BAF (Figure 6C). Indeed, performing molecular docking on
353 these mutant structures demonstrated worse binding scores and altered hexadecenal positioning
354 due to the disruption of BAF topography (Figure 6D−E). Of note, we ran clustering analysis on all
355 the docked poses for each mutant and found that the poses were sufficiently similar to be
356 clustered together with the exception of BAX^{L113M}, which still positioned one pose into the
357 shallower BAF; however, this pose had worse scoring compared to the top L113M hits.

358 To corroborate our *in silico* predictions, we generated recombinant protein for these BAF mutants
359 and tested them for BAX functionality. Several established BAX point mutants result in a deficient
360 or functionally dead protein, and so we first determined the melting temperature of our BAF
361 mutants. Compared to WT, each BAF mutant exhibited a lower melting temperature, suggesting
362 that these mutations would not be functionally deficient (Figure 6F). While the lower melting
363 temperature may also suggest reduced stability of the monomeric protein, we did not observe any
364 redistribution to oligomeric species during protein purification and storage (data not shown).
365 Furthermore, we confirmed that each BAF mutant responded to BIM activation with similar
366 kinetics and endpoint, noting only slight insensitivity of BAX^{L113M} at low BIM concentrations but

367 similar activation at high concentrations (Figures 6G, S8A). Critically, each BAF mutant
368 demonstrated complete insensitivity to hexadecenal and exhibited no synergy with BIM-primed
369 BAX (Figures 6H, S8B−C). Indeed, this result was conserved even with activating concentrations
370 of BIM (data not shown). It is worth noting that BAX[L113M] did retain some synergy of BIM and
371 hexadecenal, albeit dramatically reduced, and we suggest that this may be a consequence of a
372 shallower, but relatively intact BAF in the BAX[L113M] structure (Figure 6E). As an aside, we did
373 generate and screen candidate mutations altering the bulky BAF residues (i.e., F114 and F143),
374 but observed reduced stability, oligomerization during purification, and substantially increased
375 sensitivity to BIM, which obfuscated interpretations with hexadecenal (data not shown).
376 Interestingly, a prior study also noted that mutation of F114 is highly sensitizing,[36] and we posit
377 that substituting these bulky residues enlarges the BAF and subsequently destabilizes BAX (see
378 Discussion). Collectively, these investigations indicate that the activating mechanism of
379 hexadecenal is the ability of the aldehyde to reside in the depth of the BAF, and alteration to the
380 BAF shape or aldehyde size disrupts this fundamental interaction.

381 **Proline 168 allosterically controls the BAF and 2t-hexadecenal function**

382 Our modern understanding of the BAX structure-function relationship includes the concept of
383 allostery, in which interactions on BAX can cause structural rearrangements in distal regions. This
384 concept is observed during BIM-mediated activation, which elicits mobilization of α9 from the BC
385 groove[30], or binding of a sensitizing molecule to the hairpin pocket, which provokes exposure of
386 the α1−2 loop[33] – both structural events are hallmarks of BAX activation.[4] Recently, the structure
387 of BAX containing a mutation of proline 168 (BAX[P168G]) was described and proposed to cause
388 rotation of bulky sidechains in the allosteric α4−5 and α7−8 loops.[37] Despite identification of P168
389 as critical for BAX activation, translocation, and pore-forming ability over 20 years ago,[38] and its
390 recent identification as an arising loss-of-function mutation conferring resistance to venetoclax
391 therapy in acute myeloid leukemia,[39] a mechanistic explanation for its requirement has remained
392 elusive. We hypothesized that the alternative rotamers in bulky α8-proximal residues may
393 consequently alter the BAF and, indeed, the neck of the BAF was lost in the BAX[P168G] structure
394 (Figure 7A). Furthermore, molecular docking against the BAX[P168G] structure positioned the
395 aldehyde with the carbon chain now pivoting towards α1 residues (Figures 7A−B). Directly
396 comparison between poses of hexadecenal docked to WT and P168G structures revealed distinct
397 interaction signatures favoring interactions with α5 and α6 or α1 residues, respectively (Figure
398 7C).

399 We reasoned that disruption of the BAF in BAX[P168G] would inhibit interactions with hexadecenal.
400 Using our FLAMBE assay, we demonstrated that BIM-primed BAX[P168G] did not activate in
401 response to hexadecenal as compared to BAX[WT] (Figures 7D, S9A). Furthermore, BAX[P168G]
402 exhibited less shift in melting temperature due to hexadecenal (Figure 7E). As expected, BAX[P168G]
403 was less sensitive to BIM activation and resulted in attenuated membrane permeabilization, but
404 notably was not entirely functionally dead (Figures 7F, S9B). In contrast, BAX[P168G] demonstrated
405 no activation in response to hexadecenal and only minor synergy with BIM at activating
406 concentrations, suggesting that activation-induced molecular rearrangements are the limiting
407 factor for the synergistic function of hexadecenal (Figures 7G, S9C). As detailed by others,[37] we
408 also observed a significantly higher melting temperature in BAX[P168G] compared to BAX[WT],
409 suggesting a stabilization of the monomeric conformer (Figure 7E). Finally, we replicated our
410 apoptosis experiments in *Bax^{−/−}Bak^{−/−}* DKO MEFs transduced to stably express either BAX[WT] or
411 BAX[P168G] (Figure S9D). The DKO MEFs reconstituted with BAX[WT] exhibited greater sensitivity to

412   ectopic hexadecenal compared to BAX^{P168G}-expressing MEFs (Figure 7H). Furthermore, this
413   discrepancy was maintained in MEFs co-treated with hexadecenal and ABT-737 (Figures 7H−I).
414   Taken together, these results reveal that BAX^{P168G} is insensitive to hexadecenal and synergy with
415   BIM due to disfunction of the BAF. Furthermore, we posit that the increased flexibility in the α8−9
416   loop (by substituting a rigid proline for glycine) may also alter the mobilization of α8 and
417   subsequent BAF exposure following BIM triggering in addition to deforming the BAF structure
418   through allosteric sidechain reorganization.

419 **DISCUSSION**

420 **2t-hexadecenal non-covalently binds the BAX Actuating Funnel to potentiate BAX**
421 **activation**

422 Several decades have been devoted to characterizing the protein-protein interactions that govern
423 the BCL-2 family and mediate the onset of MOMP following pro-apoptotic signaling. More recently,
424 a growing focus on the mitochondrial contributions to potentiate MOMP have been identified,
425 including mitochondrial mass, shape or curvature, OMM-IMM junctions, mitochondrial-ER contact
426 sites, and the OMM lipid milieu and cardiolipin.[40] Additionally, the sphingolipid metabolites S1P
427 and 2t-hexadecenal were identified as the first *de facto* signaling lipid species to modulate the
428 BCL-2 effector proteins, BAK and BAX, respectively.[15] Here, we have demonstrated that
429 2t-hexadecenal directly promotes BAX activation via non-covalent interactions (Figures 1–2), and
430 cooperates with direct activators to enhance early-activation steps of monomeric BAX prior to
431 membrane interactions or oligomerization (Figure 3). We determined that 2t-hexadecenal
432 interacts within a hydrophobic funnel-shaped cavity in the core of BAX, formed residues of α1,
433 α5, α6, and capped by α8, which we now term the "BAX Actuating Funnel" or BAF, and that this
434 region is exposed and enlarged following BIM triggering (Figure 4). We identified chemical and
435 structural determinants of the hexadecenal:BAF interaction, including aldehyde length (Figure 5)
436 and BAF residues (Figure 6), and further revealed that proline 168 allosterically regulates the BAF
437 and subsequent mutation reduces BAF topography and availability (Figure 7). We therefore
438 propose a cohesive model for successive BAX activation: BIM-mediated triggering induces α9
439 mobilization as well as tandem α8 movement, resulting in accessibility of the BAF, interactions
440 with 2t-hexadecenal, and promoting subsequent conformational changes and pore formation
441 (Figure 7J).

442 In contrast, two previous studies reported that 2t-hexadecenal covalently modifies BAX cysteine
443 residues through Michael addition. One study synthesized a clickable alkyene analogue of
444 2t-hexadecenal and observed modification of C62 in cell lysates and recombinant protein[26], while
445 another study observed alkylation at C126 using recombinant BAX[23]. Both studies also
446 demonstrated that the saturated aldehyde hexadecanal was non-activating and did not modify
447 BAX. One possible explanation is the concentration of 2t-hexadecenal used, which often ranged
448 from high micromolar to millimolar ranges and liposome formulations upwards of 10%
449 2t-hexadecenal, which may have facilitated covalent modification; another is that cell lysate and
450 recombinant protein buffers contained NP-40 nonionic detergent, which directly engages
451 monomeric BAX activation.[2,41] We also cannot rule out the possibility of additional differences in
452 solvents, buffer formulations, reagents, or pH that likely affect the reaction chemistry and may
453 explain the divergent results; however, we were unable to identify a set of conditions to induce
454 modification by 2t-hexadecenal as a positive control for LC-MS analysis. Another difference
455 between studies was the BAX protein, which was either tagged (HA-tagged for overexpression or
456 His-tagged for recombinant vectors)[26] or was determined to have a molecular weight slightly
457 greater than the calculated mass of BAX (21320 Da observed compared to 21184 Da predicted)[23].
458 Perhaps these minor modifications to the BAX protein altered cysteine exposure, the neighboring
459 residues, or otherwise favored the covalent reaction mechanism.

460 Critically, we do not dispute the findings of these prior studies nor the conclusion that cysteine
461 modification modulates BAX activity.[42] There is substantial evidence that 2t-hexadecenal and α,β-
462 unsaturated aldehydes are inherently reactive molecular species that form adducts with a variety

463   of macromolecules.[22,25] In fact, over 500 proteins were identified to be modified by the
464   2t-hexadecenal analogue probe[26], suggesting that cysteine modification of BAX is not a unique
465   or selective phenomenon, which further highlights the need to individually investigate each protein.
466   In a cell, 2t-hexadecenal is promptly metabolized by FALDH/ALDH3A2 to avoid accumulation of
467   reactive fatty aldehydes, lipid peroxides, and alkylated adducts[16,43,44]; as such, cellular BAX is
468   unlikely to experience micro- or millimolar concentrations of 2t-hexadecenal and subsequent
469   modification under physiological conditions. We posit that the confluence of sphingolipid
470   metabolism, lipid transfer, and BAX apoptotic foci forming at MERCS serves to regulate the
471   availability of 2t-hexadecenal during BAX activation.[40] We also observed that short-chain alkenals
472   did not activate BAX, which aligns with a prior study that also demonstrated increased reactivity
473   with short-chain alkenals.[23] While not measured for 2t-hexadecenal or long-chain alkenals
474   specifically, it has been reported that 2t-alkenals exhibit reduced reactivity in a length-dependent
475   manner despite having similar electrophilic indices, possibly due to differences in steric
476   hinderance or relative solubility/hydrophobicity.[45,46] Therefore, we propose that while
477   2t-hexadecenal can covalently modify BAX *in vitro* and cell lysates, this likely does not represent
478   the primary mechanism promoting BAX activation, which we suggest is via non-covalent
479   interactions within the BAF.

480   **2t-hexadecenal and the gatekeeper α8 helix in BAX activation**

481   So how does 2t-hexadecenal binding to the BAF promote BAX activation? One possible
482   explanation is that residence of 2t-hexadecenal in the BAF occupies space that would otherwise
483   accommodate bulky aromatic residues of α8. Activated BAX monomers can be "reset" by anti-
484   apoptotic BCL-2 protein (e.g., BCL-xL)[47,48] and perhaps the steric interference of 2t-hexadecenal
485   prevents replacement of α8 and α9 into the BAF and BC groove, respectively. Another
486   explanation could be that binding of 2t-hexadecenal, particularly in the neck of the BAF, which
487   resides deep in the core of BAX, is inherently destabilizing to the packing of side chains and core
488   helices. Therefore, 2t-hexadecenal binding may aid separation of the core and latch domains and
489   facilitate forming multimeric conformers. Additionally, residence in the BAF may also aid BAX
490   activation by promoting exposure of the BAX BH3 residues, which are core-facing in the inactive
491   conformer, through steric interference with α2.[4,49,50]

492   Interestingly, the concept of a lipid-interacting funnel cavity capped by a gatekeeper helix is also
493   present in the only other protein known to non-covalently bind 2t-hexadecenal – FALDH. In
494   FALDH, the substrate site is a deep hydrophobic funnel capped with a short gatekeeping helix,
495   which is hypothesized to participate in substrate specificity.[51] The gatekeeper helix has several
496   aromatic residues and is stabilized through interactions with the preceding helix, which has a
497   perpendicular orientation, and a lateral loop region, in a parallel orientation (similar to BAX α7 and
498   α4–5 loop). Like BAX, the FALDH gatekeeper helix is the penultimate helix, and is followed by a
499   short linker and a C-terminal helix that serves as a transmembrane domain, orienting the entrance
500   of the funnel towards the residential membrane. Of note, FALDH functions as a symmetrical
501   homodimer with the stabilizing helix, gatekeeping helix, and transmembrane helix folding on the
502   trans subunit, bearing a striking similarity to the domain-swapped BAX dimer structure.[6] The
503   specificity of FALDH is attributed to the cooperation of the hydrophobic loop, the stabilizing helix,
504   and the gatekeeper helix that collectively surround the substrate funnel; and it is tempting to
505   speculate that the similar features in the BAX structure may likewise play a role in 2t-hexadecenal
506   recruitment and specificity.

The BAF provides structure-function insights into monomeric BAX biology

Monomeric BAX conformers must undergo substantial unfolding to adopt multimeric structures, and therefore, from a structural perspective, "activating" BAX must sufficiently destabilize the monomer to enable refolding into domain-swapped conformations. Interestingly, several features of the BAX structure support this conceptualization of activation. For example, BAX has no disulfide bonds and evolved to fold entirely through hydrophobic/hydrophilic and electrostatic interactions, which decreases the energy "hill" to transition between stable conformers (e.g., monomer to domain-swapped dimer). Additionally, cavities or voids destabilize globular proteins[52,53], and BAX studies mutating bulky core residues with smaller side chains have observed increased sensitivity to activation[36], likely due to enlarging the BAF and reducing stability[54,55]. Indeed, we observed this phenomenon when we mutated F114 or F143 (data not shown). Of note, the cavity has also been observed in the BID-BH3:BAX$^{\Delta C21}$ and BAX-BH3:BAX$^{\Delta C21}$ domain-swapped dimer structures (PDBs 4BD2 and 4BD6, respectively)[6], as well as the BH3-in-groove:BAX$^{\Delta C26}$ complexes (PDBs 4ZIF and 4ZIG)[56]; albeit the location is more central to α2, α5, and α8 (i.e., the "mouth" of the BAF), and may be expanded by the removal of α9 and adjacent residues. One interesting insight is that BAX$^{\Delta C28}$ exhibited a diminished cavity due to a shift in the α2 helix[56], suggesting that bulky residues within and proximal to α8 (e.g., F165 and W170) may aid in maintaining the cavity through interactions with α2. Additionally, we explored the role of P168 in BAF shape and availability in this work. The presence of the cavity in several solved apo and BH3-bound BAX structures strongly suggests its importance to the structure-function relationship of BAX and supports the destabilization concept of BAX activation.

Our model suggests that activation-induced mobilization of α9 also results in displacement of α8, which in turn exposes the BAF and hydrophobic core. Therefore, we propose that α8 functions as a gatekeeper helix – capping the cavity, limiting solvent exposure of hydrophobic residues, and ultimately stabilizing the monomeric conformation of BAX through interactions within the helical bundle. This model is supported by the fact that the P168G mutation, which increases flexibility in the α8−9 loop and we propose limits α8 mobility, exhibits increased protein stability as the inactive, globular monomer. Furthermore, several studies have demonstrated that disruption of α8 is deleterious to monomeric BAX stability: a proline substitution in α8 (L161P) caused oligomerization and cell death[57]; removal of α8 and α9 (BAX$^{\Delta C35}$) resulted in oligomerization[58]; C-terminal truncations (BAX$^{\Delta C21}$, BAX$^{\Delta C25}$, BAX$^{\Delta C28}$) remained monomeric but deletion of Y164 (BAX$^{\Delta C29}$) caused oligomerization[6]. Furthermore, one of our BAX$^{\alpha 8}$-locked mutagenesis strategies (BAX^{W107C,Y164C}) resulted in recombinant protein purifying primarily as oligomeric species (data not shown). Notably, W107 and Y164 are predicted to exhibit pi-stacking as are several aromatic residues localized to the α4–5 loop and α7/α8. Interestingly, these segments of BAX are the BH1 and BH2 domains, suggesting that their conservation within multidomain BCL-2 family proteins is due, at least in part, to their role in stabilizing the helical bundle via the α8 cap.

Concluding thoughts

Here, we describe a cohesive model of BAX activation, in which successive contributions of protein-protein and protein-lipid interactions promote intramolecular maturation of BAX monomers into functional oligomers. We propose that interactions between 2t-hexadecenal and the exposed BAF can occur either in the cytosol, as we have modeled herein, or at the OMM, as modeled by others[23]. Lipids play a critical role in BAX activation, both in early-activation steps as well as pore

551 formation. Interestingly, while activated BAK structures bind and incorporate lipid moieties,
552 analogous studies have not identified a similar mechanism in BAX multimers suggesting that there
553 may be a divergent mechanism.[59,60] BAX is unique in that much of its regulation occurs in solution
554 prior to membrane association and therefore the lipid contributions to BAX activation may function
555 primarily on monomeric activation instead of oligomerization. Finally, this work describes the
556 function and importance of the BAF, which had previously been identified but its significance was
557 never determined.[6,56] The BAF represents a new regulatory region that is critical for understanding
558 monomeric BAX structure-function biology as well as providing a new space for pharmacologically
559 targeting BAX. The BAF is exposed following BIM- or BID-induced BAX activation and thus we
560 suggest that BAF-targeting molecules would be particularly adept at modulating BAX in cellular
561 contexts that actively maintain direct activator BH3-only protein function (e.g., "primed" cells)
562 while being well tolerated in healthy tissues where the BAF is unexposed.

ACKNOWLEDGEMENTS

AUTHOR CONTRIBUTIONS

Conceptualization: J.D.G. and J.E.C.; methodology: J.D.G., Y.C., A.V.F., and J.N.M.; validation: J.D.G., Y.C., J.N.M., and T.M.S.; investigation: J.D.G., Y.C., M.P.A.L.-V., A.V.F., S.G.B., J.N.M., T.M.S., and N.D.P.; resources: Y.C., M.P.A.L.-V., and M.A.N.; writing: J.D.G. and J.E.C.; visualization: J.D.G.; supervision: Y.S., R.W.K., and J.E.C.; funding acquisition: J.D.G., R.W.K., and J.E.C.

COMPETING INTERESTS

The authors declare no competing interests.

583   FIGURE LEGENDS

584   Figure 1: 2t-hexadecenal induces apoptosis and membrane permeabilization by
585   cooperating with BAX

586   **(A–C)** MEFs subjected to SPARKL analysis measuring real-time labeling with fluorescently-
587   tagged Annexin V (100 µg/ml) via imaging with an IncuCyte ZOOM. Left panels: kinetics of cell
588   labeling in response to increasing concentrations of 2t-hexadecenal (2t-16) with DMSO vehicle
589   or co-treated with ABT-737 (ABT); black line reports untreated control. Right panels: endpoint
590   data of replicates at 24 hours. Data shown are the mean of technical triplicates and error bars
591   report SEM.
592   **(A)** WT MEFs (matched to *Bax*$^{-/-}$*Bak*$^{-/-}$ double knockout MEFs) were treated with 2t-16 (10, 20,
593   40 µM) and DMSO or ABT-737 (1 µM), imaged every 2 hours, and quantified for number of
594   Annexin V-positive objects.
595   **(B)** Same as in **A** with *Bim*$^{-/-}$*Bid*$^{-/-}$ double knockout MEFs.
596   **(C)** Same as in **A** with *Bax*$^{-/-}$*Bak*$^{-/-}$ double knockout MEFs.
597   **(D–I)** LUV permeabilization studies with recombinant BAX protein treated as indicated and
598   measured at regular intervals for changes in fluorescence as fluorophores are released from
599   liposomes. Grey data report LUVs solubilized with 1% CHAPS to measure maximal signal. Data
600   shown are the mean of technical replicates.
601   **(D)** BAX protein (120 nM) was combined with DMSO vehicle or 2t-16 (6.5–50 µM) followed by
602   addition of LUVs and measured by fluorescent spectroscopy.
603   **(E)** Same as in **D** with BIM-BH3 peptide (2.5 µM) added to BAX and 2t-16.
604   **(F)** Heatmap visualization of normalized endpoint LUV permeabilization data from LUVs
605   incubated with BAX (120 nM) treated with 2t-16 (6.5–50 µM) ± BIM-BH3 peptide (0.5, 2.5 µM).
606   Data summarized from Figures **S1C**.
607   **(G–H)** LUV permeabilization studies as in **D–E** with BAX (160 nM) and hexadecanal (6.5–50 µM)
608   ± BIM-BH3 peptide (2.5 µM).
609   **(I)** Heatmap visualization of normalized endpoint LUV permeabilization data as in **F** with BAX (160
610   nM) and 16CHO (6.5−50 µM). Data summarized from Figures **S1D**.
611   See also Figure S1.

612   Figure 2: 2t-hexadecenal activation of BAX is mediated by non-covalent interactions

613   **(A–B)** Alexa Fluor 647-labeled recombinant BAX^{WT} (1 nM) was incubated with CHAPS (0.002%)
614   to inhibit oligomerization, treated as indicated, and subjected to MST. Data shown are the mean
615   of replicate data and error bars report SD.
616   **(A)** Left: Timetrace thermal shift curves of BAX^{WT} titrated with 2t-16 (0.02–40 µM) and subjected
617   to MST. Right: Thermophoresis and temperature jump value for BAX^{WT} treated with a range of
618   2t-16 concentrations fitted to determine a K_D value.
619   **(B)** BAX^{WT} was treated with 2t-16 or 16CHO (0.04, 1.25, 40 µM) and MST timetrace thermal shift
620   curves were fitted using a one-step exponential function and compared using the decay (K)
621   constants normalized by the untreated BAX curve. Original data in Figure **S2C**.
622   **(C)** LC-MS of recombinant BAX^{WT} alone or incubated with 2t-16. Samples were then alkylated
623   with iodoacetamide to identify unmodified cysteine residues and trypsin digested for analysis.
624   Four cysteine-containing peptide fragments were detected. Values denote peptide abundance,
625   calculated as AUC for each peak.
626   **(D–I)** LUV permeabilization studies with recombinant BAX^{2S} protein treated as indicated and
627   measured at regular intervals for changes in fluorescence as fluorophores are released from

17

628   liposomes. Grey data report LUVs solubilized with 1% CHAPS to measure maximal signal. Data
629   shown are the mean of technical replicates.
630   **(D)** BAX^{2S} protein (100 nM) was combined with DMSO vehicle or 2t-16 (6.5–50 µM) followed by
631   addition of LUVs and measured by fluorescent spectroscopy.
632   **(E)** Same as in **D** with BIM-BH3 peptide (2.5 µM) added to BAX^{2S} and 2t-16.
633   **(F)** Heatmap visualization of normalized endpoint LUV permeabilization data from LUVs
634   incubated with BAX^{2S} (100 nM) treated with 2t-16 (6.5–50 µM) ± BIM-BH3 peptide (0.5, 2.5 µM).
635   Data summarized from Figure **S2B**.
636   **(G–H)** LUV permeabilization studies as in **D–E** with BAX^{2S} (100 nM) and hexadecanal (6.5–50
637   µM) ± BIM-BH3 peptide (2.5 µM).
638   **(I)** Heatmap visualization of normalized endpoint LUV permeabilization data from LUVs incubated
639   with BAX^{2S} (100 nM) treated with 16CHO (6.5–50 µM) ± BIM-BH3 peptide (0.5, 2.5 µM). Data
640   summarized from Figure **S2C**.
641   See also Figure S2.

642   **Figure 3: 2t-hexadecenal synergizes with BIM to induce intramolecular rearrangements**
643   **and early-activation of monomeric BAX**

644   **(A–D)** BAX was treated as indicated, combined with a TAMRA-labeled BAK-BH3 peptide
645   (BAK^{TAMRA}), and immediately subjected to FLAMBE analysis in which the association and
646   activation-induced dissociation of BAK^{TAMRA} is monitored via changes in Polarization. Left panels:
647   kinetic Polarization data; right panels: two-dimensional plot of parameterized FLAMBE data
648   comparing Tmax and endpoint Polarization metrics normalized to BAK^{TAMRA} (grey data) and the
649   vehicle-treated BAX control (black data).
650   **(A)** BAX^{WT} (60 nM) was treated with 2t-16 (2–50 µM), combined with BAK^{TAMRA} (50 nM), and
651   subjected to FLAMBE.
652   **(B)** Same as in **A** with BAX^{2S} (60 nM).
653   **(C)** Left: BAX^{2S} (60 nM) was combined with non-activating concentrations of BIM-BH3 peptide
654   (0.15 µM) and 2t-16 (4.5 µM), followed by BAK^{TAMRA} (50 nM), and subjected to FLAMBE. Right:
655   Parameterized FLAMBE data including three concentrations of 2t-16 (green: 4.5 µM; orange: 6.5
656   µM; red: 10 µM) in the absence or presence of BIM-BH3 (circle and square datapoints,
657   respectively). Annotations report the magnitude of shift between data with and without BIM-BH3.
658   **(D)** Left: Same as in **C** with an activating concentration of BIM-BH3 and three concentrations of
659   2t-16 (green: 4.5 µM; orange: 6.5 µM; red: 10 µM). Right: Parameterized FLAMBE data reporting
660   shift in samples with or without BIM-BH3. Conditions without BIM-BH3 provided in Figure **S3F**.
661   **(E)** BAX^{WT} (800 nM) was treated with BIM-BH3 (2.5, 10 µM) and 2t-16 (50 µM) for 1 hour,
662   subjected to size exclusion chromatography, and measured by 280 nm absorbance (A280) as
663   eluate flowed out of the column.
664   **(F)** Alexa Fluor 488-labeled BAX^{WT} (400 nM) was treated with 2t-16 (50 µM) and/or BIM-BH3 (10
665   µM) for 1 hour and subjected to size exclusion chromatography. Samples of fractions were
666   analyzed by fluorescence spectroscopy to track BAX. Oligomeric BAX (BAX$_O$) was generated via
667   overnight treatment with DDPC (1 mM).
668   **(G)** Same as in **F** with 16CHO (50 µM).
669   See also Figure S3.

Figure 4: 2t-hexadecenal interacts with an alpha 8 helix-gated hydrophobic cavity in the core of BAX

(A) ^{15}N-labeled BAX^{WT} (40 µM) was treated with vehicle or 2t-16 (50, 150 µM) and subjected to ^{1}H-^{15}N HSQC NMR. Chemical shift perturbations (CSPs) are plotted as a function of BAX residues. Residues exhibiting a shift greater than 1 or 2 standard deviations above the average (dotted lines) are colored light and dark purple, respectively, and indicated on the BAX structure (PDB: 1F16). The absence of a bar indicates no chemical shift difference, the presence of a proline, or the residue could not be definitively assigned.

(B) Cartoon visualization of BAX (PDB: 1F16) and the hydrophobic cavity in the BAX core formed by helices α1, α5, α6, and α7. The cavity proximal to α8 is highlighted; a distinct cavity deeper in the core between α5 and α6 is outlined. Cavity determination and visualization was performed with PyMOL using a cavity radius of 3 and a cavity cutoff of -5.5.

(C) Unbiased *in silico* rigid docking of 2t-16 against the unmodified BAX structure (PDB: 1F16) using the SwissDock web service. Results position the majority of 2t-16 poses at the α8 helix.

(D) *In silco* docking was performed as in **C** on a BAX structure with α8 removed (PDB: 1F16, Δ157–163; "BAX^{Δα8}"). Inset displays cross-section of 2t-16 docking within the hydrophobic funnel.

(E) Unmodified structure of BAX bound to a BIM-BH3 peptide (PDB: 2K7W; "BAX:BIM") with the enlarged, connected cavity visualized as in **B**.

(F) Results of 2t-16 docking on the structure of BAX:BIM with α8 removed (PDB: 2K7W, Δ157–163; "BAX^{Δα8}:BIM") as in **C**. Inset displays cross-section of ligand docking within the hydrophobic funnel.

(G) Cartoon visualization of the BAX^{α8} mutant (modified from PDB: 1F16). Residues L59 and L162 were mutated to cysteine and oxidized to form a disulfide tether immobilizing α8.

(H) Alexa Fluor 488-labeled BAX^{α8} (400 nM) was treated with 2t-16 (50 µM) and/or BIM-BH3 (10 µM) for 1 hour and subjected to size exclusion chromatography. Samples of fractions were analyzed by fluorescence spectroscopy to identify BAX-containing fractions.

(I) Left: BAX^{α8} (225 nM) was combined with non-activating concentrations of BIM-BH3 peptide (0.15 µM) and 2t-16 (4.5 µM), followed by BAK^{TAMRA} (50 nM), and subjected to FLAMBE analysis. Right: Parameterized FLAMBE data including four concentrations of 2t-16 (blue: 3 µM; green: 4.5 µM; orange: 6.5 µM; red: 10 µM) in the absence or presence of BIM-BH3 (circle and square datapoints, respectively). Annotations report the magnitude of shift between data without and with BIM-BH3. Kinetic data for all concentrations is provided in Figure **S4J**.

See also Figure S4.

Figure 5: Aldehyde length controls BAF function and BAX activation

(A) ^{15}N-labeled BAX^{WT} (40 µM) treated with 2t-16, nonenal (2t-9), or pentenal (2t-5) and subjected to ^{1}H-^{15}N HSQC NMR. Residues exhibiting significant CSPs averaged across concentrations for each of the indicated 2t-alkenal are highlighted. Each row is color-coded to report residues exhibiting shifts greater than 1 (light color) or 2 (dark color) standard deviations above the average across measurable shifts. Data summarized from Figure **S5A**.

(B) Results of unbiased *in silico* rigid docking 2t-alkenals or S1P against the full-length BAX or BAX^{Δα8} structure using the SwissDock web service. Binding modalities were inspected for positioning proximal (for BAX^{FL}) or within (BAX^{Δα8}) the BAF and reported as the percent of total poses. Visualizations of docking results provided in Figure **S6A–B**.

(C) Summary of MST analyses with BAX^{WT} incubated with 2t-alkenals of differing carbon lengths (5–13 carbons) at a range of concentrations (0.16–5 µM). The thermophoresis datapoints were fit and the slope is provided for each alkenal. Original timetrace data provided in Figure **S7A**.

716   **(D)** Parameterized data from FLAMBE studies with BAX^{2S} (60 nM) treated with 2t-alkenals of
717   differing carbon lengths (5–13, 16 carbons) at several concentrations (3–50 µM). Black and grey
718   datapoints report vehicle-treated BAX^{2S} and BAK^{TAMRA}, respectively. Original data provided in
719   Figure **S7B**.
720   **(E)** FLAMBE data trends for each of the 2t-alkenal titration from **D**.
721   **(F)** Heatmap visualization of endpoint permeabilization data from LUVs incubated with BAX^{2S}
722   (100 nM) treated with 2t-alkenals of differing carbon lengths (5–13, 16 carbons) at several
723   concentrations (6.5–50 µM). Each experiment was normalized to the matching vehicle-treated
724   BAX^{2S} condition to control for variability. Original data provided in Figure **S7C**.
725   See also Figures S5−7.

726   **Figure 6: Proximal BAF mutations disrupt 2t-hexadecenal synergy with BAX and BIM**

727   **(A)** Molecular docking and modeling of BAX$^{\Delta\alpha 8}$:BIM (PDB: 2K7W, Δ157–163) with 2t-16 using
728   Schrödinger Glide with a binding region localized to the BAF. The interaction diagram identified
729   several hydrophobic residues lining the BAF.
730   **(B)** The highest scoring pose from **A** is shown and is representative of all generated poses.
731   Surface of exposed BAF shown in grey wireframe and clipped to aid in visualization.
732   **(C)** Cartoon visualization of full-length BAX (PDB: 1F16) with BAF residues identified in **A**
733   highlighted in yellow. A virtual mutagenesis screen was performed with PyMOL to identify BAF-
734   disrupting mutations. Right: candidate side chain replacements altering the BAF are shown in red
735   and compared to the WT BAF. Cavity determination and visualization was performed with PyMOL
736   using a cavity radius of 3 and a cavity cutoff of -5.5.
737   **(D)** Molecular docking as in **A** against structures containing the indicated mutations. Generated
738   poses of 2t-16 had reduced interaction scores against mutant structures compared to the wild
739   type structure resulting from the altered BAF.
740   **(E)** The highest scoring poses from **D** are shown and representative of generated poses.
741   **(F)** The melting temperature of each mutant was measured by thermal shift differential scanning
742   fluorimetry using SYPRO orange. Statistical significance was determined by two-way ANOVA; ***
743   denotes *P* < 0.001.
744   **(G)** Heatmap visualization of normalized endpoint LUV permeabilization data for WT and BAF
745   mutants activated with a range of BIM-BH3 concentrations (0.125−2 µM). Data summarized from
746   Figure **S8A**.
747   **(H)** Heatmap visualization of normalized endpoint LUV permeabilization data from LUVs
748   incubated with the BAF mutants treated with 2t-16 (6.5–50 µM) ± BIM-BH3 peptide (0.15 µM).
749   Data summarized from Figure **S8B–C**.
750   See also Figure S8.

751   **Figure 7: Mutation of proline 168 allosterically disrupts the BAF and 2t-hexadecenal**
752   **function**

753   **(A–C)** Molecular docking and modeling of BAX$^{P168G\Delta\alpha 8}$ (PDB: 5W60, Δ157–163) with 2t-16 using
754   Schrödinger Glide with a binding region localized to the BAF.
755   **(A)** The BAX^{P168G} structure includes divergent rotamers of bulky core residues that removes the
756   neck of the BAF. The highest scoring pose is shown and is representative of generated poses.
757   Surface of exposed BAF shown in green wireframe and clipped to aid in visualization. The BAF
758   surface from WT BAX is overlayed in grey for comparison.
759   **(B)** The interaction diagram from **A** reveals that 2t-16 interacts with distinct residues, including
760   sidechains of α1.

761 **(C)** Residues interacting with 2t-16 were compared between WT and P168G BAX and colored
762 green or red, respectively, according to the number of poses and specificity for one of the isoforms.
763 Structure of BAX$^{\Delta\alpha8}$:BIM included for visualization as well as top scoring 2t-16 poses.
764 **(D)** Left: BAX^{P168G} (65 nM) was combined with non-activating concentrations of BIM-BH3 peptide
765 (0.15 µM) and 2t-16 (3 µM), followed by BAK^{TAMRA} (50 nM), and subjected to FLAMBE. Right:
766 Parameterized FLAMBE data including four concentrations of 2t-16 (blue: 3 µM; green: 4.5 µM;
767 orange: 6.5 µM; red: 10 µM) in the absence or presence of BIM-BH3 (circle and square datapoints,
768 respectively). Annotations report the magnitude of shift between data with and without BIM-BH3.
769 Empty symbols denote parameterized data for BAX^{WT} shown in Figure **S9A** and is included for
770 comparison.
771 **(E)** The melting temperature of BAX^{WT} and BAX^{P168G} ± 2t-16 (6.5−50 µM) was measured by
772 thermal shift assay using SYPRO orange and compared. Statistical significance was determined
773 by two-way ANOVA; *** denotes $P < 0.001$.
774 **(F)** Heatmap visualization of normalized endpoint LUV permeabilization data for BAX^{WT} and
775 BAX^{P168G} mutants activated with a range of BIM-BH3 concentrations (0.125−2 µM). Data
776 summarized from Figure **S9B**.
777 **(G)** Heatmap visualization of normalized endpoint LUV permeabilization data from LUVs
778 incubated with the BAF mutants treated with 2t-16 (6.5–50 µM) ± BIM-BH3 peptide (0.15 µM).
779 Data summarized from Figure **S9C**.
780 **(H–I)** *Bax$^{-/-}$Bak$^{-/-}$* double knockout MEFs reconstituted to express BAX^{WT} or BAX^{P168G} were
781 subjected to SPARKL analysis measuring real-time labeling with fluorescently-tagged Annexin V
782 (100 µg/ml) via imaging with a Cytation 7. Data are reported as positive events per image.
783 **(H)** Kinetics of cell death for reconstituted MEFs treated with 2t-16 (10−30 µM) and co-treated
784 with DMSO vehicle or ABT-737 (1 µM); black lines report vehicle control. Data are the mean of
785 replicates and error bars are omitted for visualization.
786 **(I)** Comparison of Annexin V labeling at 18 hours for parental *Bax$^{-/-}$Bak$^{-/-}$* MEFs and BAX^{WT} or
787 BAX^{P168G} reconstituted MEFs. Data shown are the mean of technical replicates and error bars
788 report SEM.
789 **(J)** A cohesive model of protein and lipid contributions to BAX activation. A cross section of BAX
790 is illustrated to visualize changes to the hydrophobic funnel shape and accessibility (highlighted
791 in pink).
792 See also Figure S9.

METHODS

Experimental Models

Bacterial cell lines
For recombinant protein generation, One Shot™ BL21 (DE3) Chemically Competent *E. coli* were purchased from Invitrogen/Thermo Fisher Scientific (Cat. No. C600003). Cells were grown in BD Difco™ Terrific Broth (Cat. No. BD243820, Thermo Fisher Scientific) media supplemented with 1% glycerol at 37°C with shaking at 220 rpm.

Cell lines
$Bax^{+/+}Bak^{+/+}$ and $Bax^{-/-}Bak^{-/-}$ SV40-transformed MEFs were obtained from ATCC (Manassas, VA, USA); $Bim^{-/-}Bid^{-/-}$ SV40-transformed MEFs were provided by Dr. Douglas Green (St. Jude Children's Research Hospital); $Bax^{-/-}Bak^{-/-}$ double knockout MEFs reconstituted to express wild type or P168G BAX were provided by Dr. Evripidis Gavathiotis (Albert Einstein College of Medicine) and BAX expression was confirmed by western blot and GFP positivity from the pBabe IRES-GFP vector backbone. Cells were cultured in high-glucose DMEM (Cat. No. 10-017-CV, Corning, Manassas, VA, USA) containing 10% FBS (Cat. No. 10438-026, Life Technologies, Carlsbad, CA, USA), 2 mM L-glutamine (Cat. No. 25030-081, Life Technologies, Carlsbad, CA, USA), and 1× Penicillin/Streptomycin (Cat. No. 10378-016, Life Technologies, Carlsbad, CA, USA), and grown in humidified incubators at 37°C with 5% CO2. All cell cultures were maintained in mycoplasm-free conditions as verified by the HEK-Blue Detection Kit (Cat. No. hb-det2, Invivogen, San Diego, CA, USA).

Recombinant protein and peptides

Expression vectors and site-directed mutagenesis
Recombinant human BAX was expressed and purified using an intein-chitin binding domain (CBD) tag from a pTYB1 vector (BAX cDNA inserted into Nde/SapI cloning site, with a C-terminal tag).[49] BAX mutants (e.g., C62S and C126S double mutant, BAX^{2S}; L59C, C62S, C126S, and L162C quadruple mutant, $BAX^{\alpha8}$) were generated by site-directed mutagenesis of the WT construct using oligos provided in the Key Resource Table. Amplification of the *de novo* plasmids was accomplished using CloneAmp HiFi PCR Premix (Cat. No. 639298, Takara Bio, Mountain View, CA, USA) and thermo-cycled as follows: 1× [98°C for 2 minutes]; 30× [98°C for 10 seconds, 55°C for 30 seconds, 72°C for 8 minutes]; and 1× [72°C for 10 minutes]. Parental plasmids were digested by 1 µl DpnI enzyme (Cat. No. R0176, New England Biolabs, Ipswich, MA, USA) at 37°C for 15 minutes, followed by purification using the QIAquick PCR Purification Kit (Cat. No. 28104, Qiagen, Hilden, Germany). Sequences were verified by Genewiz Sanger sequencing using the Universal T7 primer (5'-TAATACGACTCACTATAGGG-3').

Recombinant BAX expression and purification
One Shot™ BL21 (DE3) chemically competent *E. coli* (Cat. No. C601003, Thermo Fisher Scientific) were transformed with the pTYB1-BAX construct in LB broth and grown on agar plates supplemented with 100 µg/mL carbenicillin at 37°C. Starter cultures were grown in Terrific Broth (TB) supplemented with 0.4% glycerol and 100 µg/mL carbenicillin at 30°C for 14–16 hours to an optical density at 600 nm (OD_{600}) of approximately 1.5; then diluted with 4× volume of TB broth and expanded at 37°C for 3–4 hours until the culture achieves a target OD_{600} of 2–3. Recombinant BAX expression was induced with 1 mM IPTG at 30°C for 6 hours. Bacteria were pelleted, resuspended in lysis buffer (50 mM K_2PO_4, 50 mM NaH_2PO_4, 500 mM NaCl, 1 mM EDTA, 0.1

836   mM AEBSF) supplemented with a Pierce protease inhibitor tablet (Cat. No. A32965, Thermo
837   Fisher Scientific), and lysed with a probe sonicator (e.g., Dismembrator 505, Thermo Fisher
838   Scientific) for 20 minutes. Lysates were centrifuged at 42,000 ×*g* at 4°C for 1 hour to pellet debris
839   and recombinant intein-CBD-tagged BAX was captured from the supernatant by chitin affinity
840   chromatography at 4°C according to the manufacturer's instructions (Cat. No. S5551, New
841   England Biolabs, Ipswich, MA, USA). On-column intein cleavage of the CBD tag was achieved
842   by incubation with DTT (50 mM) at 4°C for at least 16 hours, followed by elution in Gel Filtration
843   Buffer (20 mM HEPES [pH 7.4], 150 mM NaCl). Recombinant BAX protein (now without a tag or
844   exogenous residues) was further purified by size-exclusion chromatography using Gel Filtration
845   Buffer on a HiLoad 16/600 or 26/600 Superdex 200 pg column (Cat. No. 28989335, Cytiva) using
846   an ÄKTA pure™ 25 L1 (Cat. No. 29018225, Cytiva) at 4°C according to the manufacturer's
847   instructions. Fractions containing BAX protein were combined and concentrated using Amicon
848   Ultra-4 centrifugal filter (Cat. No. UFC801024, Millipore Sigma) to a stock concentration of ~30
849   μM, prior to snap freezing with liquid nitrogen, and storage at -80°C. A detailed version of this
850   protocol has been published.[61]

851   *Oxidizing disulfide tether BAX mutants*
852   For the BAX$^{\alpha8}$ mutant, the nascent protein was purified as the reduced form due to incubation
853   with DTT during on-column intein cleavage; to generate a disulfide tether ("locked BAX$^{\alpha8}$"), BAX
854   protein was oxidized in 1 mM Dichloro(1,10-Phenanthroline) Copper (II) (Cat. No. 362204,
855   Millipore Sigma-Aldrich) at 4°C for 15 minutes, purified by Superdex 75 Increase 10/300 GL
856   column (Cat. No. 29148721, Cytiva), and only monomeric species were pooled and concentrated
857   to make protein stocks.

858   *Other reagents*
859   Additional recombinant proteins and peptides were purchased from commercial sources: 5-
860   TAMRA labeled BAK-BH3 (Cat. No. AS-64590, AnaSpec); recombinant Bcl-xL$^{\Delta C}$, aa 2-212 (Cat.
861   No. 894-BX, R&D Systems); BIM-BH3, Peptide IV (Cat. No. AS-62279, AnaSpec).

862   **Lipid aldehyde preparation**

863   2-trans-hexadecenal (2t-hexadecenal) was purchased in powder form (Cat. No. 857459P, Avanti
864   Polar Lipids) and reconstituted in pre-warmed (37°C) anhydrous DMSO (Cat. No. D12345,
865   Thermo Fisher Scientific) to a concentration of 50 mM using a Hamilton syringe. The reconstituted
866   2t-hexadecenal was aliquoted into single-use glass aliquots and stored at -80°C. To avoid
867   precipitation/coagulation of 2t-hexadecenal, stocks were serially diluted first in pre-warmed
868   DMSO, then diluted into pre-warmed aqueous assay buffer to use as a stock for the experiment.
869   This was typically accomplished as follows: 2.5 μl of 50 mM 2t-hexadecenal stocks were two-fold
870   diluted four times in DMSO (to 40 μl of 3.13 mM), then diluted twice in the selected assay buffer
871   (first with 40 μl, then with 45 μl) to achieve a working stock of 125 μl of 1 mM 2t-hexadecenal in
872   32% DMSO/buffer. Working stocks of 1 mM 2t-hexadecenal were placed in a water bath sonicator
873   for 15 minutes to aid in solubilization and then further diluted to the desired concentration and
874   acceptable DMSO background for experiments. For cell death experiments, 2t-hexadecenal was
875   prepared in 0% FBS media to prevent binding to serum proteins.

876   Hexadecanal (16:0 aldehyde) was purchased as 1 mg/ml (4.16 mM) in methylene chloride
877   solution (Cat. No. 857458M, Avanti Polar Lipids), aliquoted into 25 μl, and stored at -80°C. Prior
878   to use, hexadecanal was first diluted with pre-warmed DMSO to a concentration of 3 mM, then
879   diluted to 1 mM with pre-warmed assay buffer of choice, sonicated for 15 minutes, and then further

880 diluted for experiments. The remaining alkenals was purchased in liquid form (see Key Resource
881 Table), and their molar concentrations were calculated based on their density, purity, and
882 molecular weight. Short-chain alkenals (2t-5 – 2t-10) were diluted with DMSO to a stock
883 concentration of 1 M, aliquoted, and stored at -80°C. Prior to use, stocks were further diluted with
884 DMSO to 320 mM and then in assay buffer to a final concentration of 1 mM with 32% DMSO (v/v).
885 Long-chain alkenals (2t-11 – 2t-13) were more likely to coagulate and thus were prepared
886 following the exact same procedure as the 2t-hexadecenal preparation.

Real-time live-cell detection of apoptosis (SPARKL)

Cell culture and treatments
889 MEFs were seeded at $2–4 × 10^3$ cells per well in 96-well tissue culture treated plates and left to
890 adhere for 18–24 hours. Prior to live-cell imaging, growth media was replaced with phenol red-
891 free DMEM as follows: first, 50 µl (50% total volume) of 0% FBS DMEM containing
892 2t-hexadecenal treatments was added to wells for 15−30 minutes; next, 50 µl of 10% FBS DMEM
893 containing additional treatments and fluorescently-labelled Annexin V (50 nM or ~1.8 ng/µl) was
894 added to wells. Recombinant Annexin V was generated in-house as previously described.[20,62,63]
895 Immediately following treatments, plates were subjected to real-time fluorescence microscopy,
896 automated data collection, and analysis.

Data acquisition and event detection with an IncuCyte ZOOM
898 SPARKL experiments performed using an IncuCyte ZOOM (Model 4459, Sartorius, Göttingen,
899 Germany) were housed in a humidified tissue culture incubator maintained at 37°C with 5% CO_2.
900 Images were collected every 2 hours for 24 hours using a 10× objective, and a single field of view
901 was collected per well. Bright field and green channels (Ex: 440/80 nm; Em: 504/44 nm;
902 acquisition time: 400 ms) were collected at 1392 × 1040 pixels at 1.22 µm/pixel. Automated event
903 detection was accomplished using the ZOOM software (v2018A) and user-defined processing
904 definition using images collected using the relevant cell lines and fluorescent reporters.
905 Processing definition settings were as follows: Parameter, Top-Hat; Radius (µm), 25; Threshold
906 (RFU), 3; Edge Sensitivity, -30; Area ($µm^2$), >100. Kinetic data are graphed as the calculated
907 events per well metric provided by the ZOOM software. The y-axis scale was determined for each
908 experiment using parallel internal control treatments to assess maximal apoptotic death. Data are
909 the mean of replicates and are representative of at least three repeated and reproduced assays.
910 A detailed explanation of this method[20] and protocol[64] have been published.

Data acquisition and event detection with a Cytation 7
912 SPARKL experiments performed using a Cytation 7 equipped with an inverted imager (Model
913 CYT7UW-SN, BioTek/Agilent, Santa Clara, CA, USA) tethered to a BioSpa 8 automated incubator
914 (Model BIOSPAG-SN, BioTek/Agilent, Santa Clara, CA, USA), where cells were maintained in a
915 humidified environment at 37°C with 5% CO_2. Bright field and red channel images were collected
916 every 2 hours for at least 24 hours using a 10× objective with a 75% wide field of view crop (1045
917 µm × 1045 µm), and a single field of view was collected per well using a laser autofocus (Part No.
918 1225010). Bright field images were acquired with the following settings: LED intensity, 7;
919 Integration Time, 100 msec; Camera Gain, 19. Red channel images (Ex: 586/18 nm; Em: 647/57,
920 Part No. 1225102) were acquired with the following settings: LED intensity, 8; Integration Time,
921 20 msec; Camera Gain, 19. Automated red event detection was accomplished using the Gen5
922 software (v3.12) and a cellular analysis data reduction profile with the following settings:
923 Threshold, 5000 RIU; Background, Dark; Split Touching Objects, yes; Fill holes, yes; Background
924 Flattening Size, auto (270 µm); Image Smoothing Strength, 0; Background Percentage, 5%;

925 Minimum Object Size: 5 µm; Maximum Object Size: 90 µm. Kinetic data are graphed as events
926 per image. The y-axis scale was determined for each experiment using parallel internal control
927 treatments to assess maximal apoptotic death. Data are the mean of replicates and are
928 representative of at least three repeated and reproduced assays.

929 **Large unilamellar vesicle (LUV) permeabilization assays**

930 *LUV composition and preparation*
931 LUVs and permeabilization assays were prepared as similarly described.[9,65] Briefly, chicken egg
932 phosphatidylcholine (Cat. No. 840051C, Avanti Polar Lipids), chicken egg
933 phosphatidylethanoloamine (Cat. No. 840021C, Avanti Polar Lipids), porcine brain
934 phosphatidylserine (Cat. No. 840032C, Avanti Polar Lipids), bovine liver phosphatidylinositol (Cat.
935 No. 840042C, Avanti Polar Lipids), and cardiolipin (18:1) (Cat. No. 710335C, Avanti Polar Lipids)
936 were combined at a ratio of 48:28:10:10:4 (5 mg total), dried under N_2 gas, and resuspended in
937 500 µl LUV buffer (10 mM HEPES [pH 7], 200 mM KCl, 5 mM $MgCl_2$, 0.2 mM EDTA) containing
938 a polyanionic dye (12.5 mM ANTS: 8-aminonaphthalene-1,3,6-trisulfonic acid) and cationic
939 quencher (45 mM DPX: p-xylene-bis-pyridinium bromide) using a water bath sonicator.
940 Unilamellar vesicles were formed by 31 extrusions of the suspension through 1.0 µm
941 polycarbonate membranes (Cat. No. 610010, Avanti Polar Lipids, Alabaster, AL, USA). The
942 unincorporated DPX and ANTS were removed by using a 10 ml Sepharose S-500 gravity flow
943 column. LUVs were used within 2 weeks of preparation to avoid significant liposome degradation.

944 *LUV assays*
945 Working stocks of recombinant proteins, peptides, and lipids were prepared in LUV buffer at 4×
946 their intended final concentrations. LUVs from the preparation stock (20×) were diluted five-fold
947 in LUV buffer to generate a working stock (4×) for assays (equivalent to each sample receiving 5
948 µl undiluted LUVs). In a black opaque 96-well plate, lipids or peptide titrations were generated via
949 in-well serial dilutions and buffer was added to any control wells requiring volume compensation.
950 Samples were assayed in 100 µl total volume with 25 µl of each component sequentially added
951 to achieve desired 1× concentrations. A typical assay was prepared as follows: 25 µl of titrant is
952 prepared in the well; then 25 µl of peptide, reagent, or buffer is added; then 25 µl of recombinant
953 BAX; and finally, 25 µl of diluted LUVs. Plates were immediately subjected to fluorescence
954 analyses for 90 minutes using either a Synergy H1 or Cytation 5 multi-mode microplate reader
955 (BioTek/Agilent, Santa Clara, CA, USA) using parameters listed in the table below. Kinetic data
956 represents the mean of triplicate samples and are representative of at least three repeated and
957 reproduced assays using separate protein aliquots and LUV preparations. Every assay included
958 a 1% CHAPS positive control to determine maximum signal. Normalized endpoint data (%
959 permeabilization) were calculated in Prism (Graphpad) using the minimum value of the buffer
960 control (as 0%) and the mean value of LUVs solubilized in 1% CHAPS (as 100%) measured
961 during the entire assay (see Equation 1). Appropriate concentrations of BAX were determined by
962 extensive protein titrations for each preparation of recombinant protein and LUVs; typically the
963 highest BAX concentration exhibiting minimal permeabilization was selected for subsequent
964 assays to ensure adequate signal and dynamic range for activation studies.

965 Table 1: Parameters for LUV permeabilization assays

Reader	BioTek Synergy H1 or Cytation 5 multi-mode plate reader
Read interval	55 seconds
Total read time	90 minutes

Protocol	37°C; 2 second linear shake; read
Excitation	355/20 nm
Emission	520/20 nm
Gain (voltage)	100
Optics position	Top
Read height	5.5 mm
Assay plate	black polystyrene 96-well (Corning #3915)
LUV buffer	10 mM HEPES (pH 7), 200 mM KCl, 5 mM MgCl$_2$, 0.2 mM EDTA

966   Equation 1: LUV data normalization

967    $$\% \text{ permeabilization} = \left(\frac{F - F_{100}}{F_{100} - F_0} \right) \times 100$$

968   **Microscale thermophoresis**

969   MST experiments were carried out on a NT.115 (NanoTemper GmbH, Munich, Germany)
970   instrument and performed in MST buffer (50 mM Tris-HCl pH 7.4, 150 mM NaCl, 10 mM MgCl$_2$,
971   0.05% Tween-20). K_D values were calculated using the NanoTemper software. The recombinant
972   human BAX protein was labeled with Alexa Fluor-647 NHS ester by incubating 60 µM of the
973   fluorescent dye with a 20 µM of BAX protein for 30 minutes in the dark. The labeling mixture was
974   subsequently applied to a G-25 gravity flow column (GE Healthcare) that had been equilibrated
975   with MST buffer. After elution from the G-25 column, the concentration of the labeled protein was
976   quantified spectrophotometrically, snap frozen in liquid nitrogen, and stored as single use aliquots
977   at -80°C. Labeled BAX protein was treated with 0.002% CHAPS to prevent activation-induced
978   BAX aggregation upon ligand binding. Curve fitting was conducted using Prism (Graphpad) and
979   only applied to X values from 5−35 seconds using Equation 2, and the K constant was calculated
980   using Equation 3.

981   Equation 2: One-phase decay function for MST data fitting

982    $$Y = \left(Y_0 - Y_{\text{Plateau}}\right)\left(e^{-KX}\right) + Y_{\text{Plateau}}$$

983   Equation 3: Decay constant function

984    $$K = \frac{-ln\left(\dfrac{Y - Y_{\text{Plateau}}}{Y_0 - Y_{\text{Plateau}}}\right)}{X}$$

985   **Liquid chromatography-mass spectrometry (LC-MS)**

986   *Sample preparation and handling*
987   Working stock of recombinant BAX protein and 2t-hexadecenal were prepared in Gel Filtration
988   Buffer. 30 µl of 5 µM recombinant BAX (~3 µg) was treated as indicated and incubated at 37°C
989   for 2 hours. Samples were then reduced in 8 M urea buffer (with 50 mM NH$_4$HCO$_3$, 10 mM TCEP)
990   at 57°C for 1 hour, and alkylated in the dark with 30 mM iodoacetamide for 30 minutes at 25°C.
991   Samples were then digested using 1:100 (w/w) trypsin at 37°C for 4 hours, with an additional
992   round of 1:100 trypsin at 37°C for 16–18 hours. After proteolysis, the peptide mixtures were
993   desalted by self-packed stage-tips or Sep-Pak C18 columns (Waters) and analyzed with a

994 Vanquish Neo UHPLC System that is coupled online with a Orbitrap Exploris 480 mass
995 spectrometer (Thermo Fisher). Briefly, desalted Nb peptides were loaded onto an analytical
996 column (C18, 1.7 µm particle size, 150 µm × 5 cm; IonOpticks) and eluted using a 20 minute
997 liquid chromatography gradient (3–10% B, 0–2 minutes; 10–40% B, 2–12 minutes; 40–80% B,
998 12–14 minutes; 3% B, 14–20 minutes). Mobile phase A consisted of 0.1% formic acid (FA), and
999 mobile phase B consisted of 0.1% FA in 80% acetonitrile (ACN). The flow rate was 1 µl/minute.
1000 The Orbitrap Exploris 480 instrument was operated in the data-dependent mode, where the top
1001 20 most abundant ions (mass range 200–1800, charge state 2–6) were fragmented by high-
1002 energy collisional dissociation (HCD). The target resolution was 120,000 for MS and 15,000 for
1003 tandem MS (MS/MS) analyses. The maximum injection time for MS/MS was set at 100 ms.

1004 *Proteomic data analysis*
1005 Raw data collected by LC-MS was searched against the Uniprot reviewed Human protein
1006 sequences database retrieved on 01 March 2024 with decoys and common contaminants
1007 appended using FragPipe (v22.0). A labile search was performed in MSFragger[66] without
1008 diagnostic and Y ions specified. Mass offsets were set restricted to cysteines. The offset list was
1009 set at 0 (no modification) and 238.22967 (monoisotopic mass of 2t-hexadecenal) and replacing
1010 the fixed cysteine carbamidomethylation with a variable one. "Write calibrated MGF" was turned
1011 on for the PTM-Shepherd[67] diagnostic feature mining module, and "Diagnostic Feature Discovery"
1012 in PTM-Shepherd was enabled with default parameters. Peptide and protein levels were
1013 performed using label-free quantification (LFQ) algorithms in IonQuant[68]. After MS search with
1014 MSFragger, raw files and identification files were imported into PDV[69]
1015 (https://github.com/wenbostar/PDV) for MS spectra annotation.

Thermal Shift Differential Scanning Fluorimetry

1017 Working stock of recombinant BAX proteins, SYPRO Orange dye (Cat. No. S6650, Thermo
1018 Fisher Scientific), and 2t-hexadecenal were prepared in gel filtration buffer. The assay was
1019 performed in 100 µl 96-well PCR plates using a total assay volume of 50 µl. 20 µl of 2.5×
1020 2t-hexadecenal titrations were generated via in-well serial dilutions and buffer was added to any
1021 control wells requiring volume compensation. 20 µl of 2.5 µM BAX and 10 µl of 20× SYPRO
1022 Orange were sequentially added to the wells, thoroughly mixed by pipetting, and the plate was
1023 centrifuged to recollect sample in the bottom of the well and remove any trapped bubbles. The
1024 PCR plate was then sealed with optically clear adhesive sheet and subjected to fluorescence
1025 spectroscopy using an Applied Biosystems ViiA7 real-time PCR instrument (Thermo Fisher
1026 Scientific). Temperature started at 25°C and increased to 95°C at a rate of 1% per minute. Data
1027 was collected as normalized fluorescence at each step of the thermal ramp and the melting
1028 temperature was determined as the maximum first derivative value. Data shown are the average
1029 of at least four replicates and error bars denote the SEM.

Fluorescence polarization ligand assay to monitor BAX early-activation (FLAMBE)

1031 *Assay setup*
1032 Working stocks of recombinant BAX protein, peptides, and lipids were prepared in 0.5× PBS
1033 buffer at 4× their intended final concentrations. 5-TAMRA labeled BAK-BH3 peptide (Cat. No. AS-
1034 64590, AnaSpec) was diluted to a 200 nM working stock (4×). In a black opaque 96-well plate,
1035 lipids or peptide titrations were generated via in-well serial dilutions and buffer was added to any
1036 control wells requiring volume compensation. Samples were assayed in 100 µl total volume with
1037 25 µl of each component sequentially added to achieve desired 1× concentrations. A typical assay

1038   was prepared as follows: 25 µl of titrant is prepared in the well; then 25 µl of peptide, reagent, or
1039   buffer is added; then 25 µl of recombinant BAX; and finally, 25 µl of BAK[TAMRA]. Plates were
1040   immediately subjected to spectrometry analyses for 60 minutes using a Synergy H1 multi-mode
1041   microplate reader equipped with a polarization filter (BioTek/Agilent, Santa Clara, CA, USA) using
1042   parameters listed in the table below. Polarization (expressed as milli-Polarization (mP) units) is
1043   derived from measured parallel and perpendicular emission intensities (I) and was calculated by
1044   the Gen5 software (BioTek/Agilent); Polarization can also be calculated manually using Equation
1045   2. Kinetic data represents the mean of triplicate samples and are representative of at least three
1046   repeated and reproduced assays using separate protein aliquots. Appropriate concentrations of
1047   BAX and peptides were determined by extensive protein titrations for each preparation of
1048   recombinant protein; typically, the highest BAX concentration exhibiting no BAK[TAMRA] dissociation
1049   was selected for subsequent assays to ensure adequate signal and dynamic range for activation
1050   studies. Similarly, concentrations of direct activators were selected from extensive titration
1051   experiments to determine the appropriate concentration for each experimental setup.

1052   *Kinetic FP data parameterization*
1053   Parameterized FLAMBE data was derived from the average of replicates to reduce data noise.
1054   For each condition, Tmax was identified as the timepoint with the highest Polarization and EP
1055   was the endpoint Polarization value recorded. Tmax of the BAK[TAMRA] control or any sample
1056   exhibiting no binding kinetics during the assay was set to 0 to avoid misidentification due to noise.
1057   Each parameterized metric was normalized to metrics from the BAK[TAMRA] and BAX control
1058   conditions, as 0 and 1 respectively. The shift magnitude of parameterized FLAMBE data was
1059   calculated using the distance between conditions without and with BIM-BH3 treatment (see
1060   Equation 3). Area under the curve (AUC) was calculated using Prism (Graphpad) and normalized
1061   to the controls. A detailed explanation of this method[8] and protocol[70] have been published.

1062   *Competition FP assay*
1063   BCL-xL competitive binding FP assays were conducted similarly to FLAMBE assays with some
1064   modifications. BCL-xL, 2t-hexadecenal, and BAK[TAMRA] were prepared as 4× working stocks in a
1065   modified FP assay buffer (20 mM sodium phosphate buffer [pH 7.4], 50 mM NaCl, 1 mM EDTA,
1066   0.05 % pluronic F-68).[71] 2t-hexadecenal titrations were prepared in-well and diluted with 25 µl
1067   buffer; separately, recombinant BCL-xL and BAK[TAMRA] stocks are combined at a 1:1 volume ratio
1068   (resulting in a 2× stock) and 50 µl is added to sample wells immediately followed by spectrometry.

1069   Table 2: Parameters for FP assays

Reader	BioTek Synergy H1 multi-mode plate reader
Filter Cube	red FP polarizer filter set (#8040562)
Read interval	30 seconds
Total read time	60 minutes
Protocol	25°C; 2 second double orbital shake; read
Excitation	530/25 nm
Emission	590/35 nm
Mirror	570 nm
Gain (voltage)	50
Optics position	Top
Read height	7.0 mm
Assay plate	black polystyrene 96-well (Corning #3915)

FLAMBE buffer	0.5× PBS
Anti-apoptotic FP buffer	20 mM phosphate buffer (pH 7.4), 50 mM NaCl, 1 mM EDTA, 0.05 % pluronic F-68

1070   Equation 2: Polarization calculation

1071 $$mP = \left(\frac{I_{parallel} - I_{perpendicular}}{I_{parallel} + I_{perpendicular}} \right) \times 1000$$

1072   Equation 3: Distance equation for parameterized FLAMBE data

1073 $$\Delta s = \sqrt{(\Delta Tmax)^2 + (\Delta EP)^2}$$

1074   Fluorescent size-exclusion chromatography

1075   Alexa Fluor™ 488 NHS ester (AF488)-labeled BAX was generated according to the
1076   manufacturer's instructions (Thermo Fisher Scientific, Cat. No. A20000) at a 20:1 dye:protein
1077   molar excess. Excess dye was removed by gel filtration with a Superdex 75 Increase 10/300 GL
1078   column (Cat. No. 29148721, Cytiva) equilibrated with Gel Filtration Buffer using an ÄKTA pure™
1079   25 L1 (Cat. No. 29018225, Cytiva) at 4°C according to the manufacturer's instructions. 0.5 ml
1080   fractions were collected and fractions containing monomeric AF488-labelled BAX were combined,
1081   quantified, aliquoted, and stored at -80°C. For experiments, 600 µl of 400 nM 488-labelled BAX
1082   was treated as indicated at 25°C for 1 hour and protected from light. Following treatment, BAX
1083   was subjected to size exclusion chromatography using the above parameters. For detection, 0.2
1084   ml of eluate from the indicated fractions was transferred to a black 96 well-plate and analyzed for
1085   fluorescence by a Cytation 5 multi-mode plate reader (BioTek/Agilent, Santa Clara, CA, USA)
1086   using the following parameters: Excitation, 495/10 nm; Emission, 520/10 nm; Gain (volage), 100.

1087   2D HSQC NMR spectroscopy

1088   ^{15}N-labeled BAX protein was prepared at 40 µM in 15 mM sodium phosphate (pH 7.0), 50 mM
1089   NaCl. Data were acquired on Bruker 600-MHz spectrometer equipped with a cryoprobe. Two-
1090   dimensional ^{1}H-^{15}N correlation spectra were acquired at 25°C using standard Bruker pulse
1091   sequences using 128 scans, 2,048 × 200 complex points and spectral windows of 14 p.p.m. × 35
1092   p.p.m. in the ^{1}H and ^{15}N dimensions, respectively. Spectra were processed using TOPSpin
1093   (Bruker Biospin, MA, USA) and analyzed with CARA software[72] (cara.nmr.ch). The weighted
1094   average chemical shift perturbation (CSP) difference (Δδ) was calculated using Equation 1. The
1095   absence of a value indicates no CSP difference, the presence of a proline, or a residue that is
1096   overlapped or missing and therefore not used in the analysis. The significance threshold for CSPs
1097   was calculated based on the average chemical shift across all measurable residues plus 1 or 2
1098   standard deviations, in accordance with standard methods. Mapping of CSP data onto the BAX
1099   structure (PDB: 1F16) was performed with PyMOL (Schrödinger, LLC).

1100   Equation 4: CSP difference equation

1101 $$\Delta\delta = \sqrt{\frac{(\Delta^1H)^2 + 0.2*(\Delta^{15}N)^2}{2}}$$

1102 **_In silico_ docking and molecular modeling**

1103 _Unbiased docking simulations_
1104 The molecular interactions between the alkenals and BAX were modeled using the EADock DSS
1105 version of the SwissDock webserver (www.swissdock.ch).[73,74] The structure PDB files and the
1106 alkenal mol2 files were obtained from the Protein Data Bank and the ZINC database, respectively
1107 (see Table 3). Output files were split into individual clusters and visualized using PyMOL
1108 (Schrödinger, LLC). Quantification of alkenal binding was accomplished by manual inspection of
1109 each cluster group and the total number of binding modality outputs for each job. Cavity
1110 determination and visualization was performed with PyMOL using a cavity radius of 3 and a cavity
1111 cutoff of -5.5; additional spaces were excluded to enhance visualization.

1112 _Virtual mutagenesis and molecular docking_
1113 Virtual mutagenesis of BAX structures was performed using the mutagenesis wizard in PyMOL
1114 (v3.1, Schrödinger, LLC) and selecting rotamers that did not conflict with surrounding sidechains;
1115 the resulting structures were utilized in downstream investigations. NMR-guided molecular
1116 docking of 2t-hexadecenal on BAX was performed using Glide (v2023-1 build 128, Schrödinger,
1117 LLC) with extra precision (XP) and a receptor grid generated in the center of the BAF (13 × 13 ×
1118 13 Å inner box, 10 Å outer box), with no additional constraints. Wild type and mutant structures
1119 had α8 residues (157−163) removed and were prepared using the Protein Prep Wizard, assigning
1120 partial charges with EPIK (Schrödinger, LLC), and aligned against the 1F16 structure to ensure
1121 consistency of BAF coordinates for grid generation. The 2t-hexadecenal structure was converted
1122 to 3D and prepared for docking using LIGPREP (v2023-1 build 128, Schrödinger, LLC). The
1123 lowest energy docking pose is visualized, was representative of all output poses, and various
1124 scoring metrics are reported. Interaction fingerprints were generated for residues exhibiting
1125 overall interaction with any of the output poses. WT and P168G BAX interaction comparisons
1126 were calculated as the fraction of total poses interacting with a residue, relative to the
1127 WT:2t-hexadecenal interaction, and color-coded for visualization in PyMOL (Schrödinger, LLC).
1128 Interaction diagrams were generated and exported from MAESTRO (Schrödinger, LLC) and then
1129 redrawn in Inkscape (www.inkscape.org) to aid in visualization.

1130 Table 3: List of resources for structural investigations

Structure	_Identifier_
BAX	PDB: 1F16[49]
BAX:BIM-BH3	PDB: 2K7W[30]
BAX-P168G	PDB: 5W60[37]
2t-hexadecenal	ZINC08217876
hexadecanal	ZINC08216082
2t-pentenal	ZINC02031161
2t-hexenal	ZINC01531148
2t-heptenal	ZINC02017189
2t-octenal	ZINC02013450
2t-nonenal	ZINC01571215
2t-decenal	ZINC01571216
2t-undecenal	ZINC01849946
2t-dodecenal	ZINC01589935
2t-tridecenal	ZINC01613339

SDS-PAGE and Western Blotting

Bax⁻/⁻Bak⁻/⁻ MEFs, or MEFs reconstituted to express WT or P168G BAX, were harvested with 0.25% Trypsin-EDTA and pelleted at 800× g for 5 minutes. Cells were lysed with 1× RIPA lysis buffer supplemented with protease inhibitors (HALT Tablet, Cat. No. 87786) and phosphatase inhibitors (ApexBio, Cat. No. k1015b) on ice for 20 minutes, pelleted at 21,000× g for 10 minutes at 4°C, and supernatant was collected for protein quantification by BCA assay (Cat. No. 23225, Thermo Fisher Scientific, Waltham, MA, USA) according to the manufacturer's protocol. Sample concentrations were equilibrated in lysis buffer, combined with 4× Laemmli sample loading buffer supplemented with DTT, subjected to SDS-PAGE in a 12.5% polyacrylamide gel, and transferred to nitrocellulose by standard western blot conditions. Membranes were blocked in 5% milk in 1× TBS buffer supplemented with 0.1% Tween-20, incubated with primary antibodies (1:500-1000 in blocking buffer; incubated for 16−18 hours at 4°C) and secondary antibodies (1:4000 in blocking buffer; incubated for 1 hour at 25°C), followed by standard enhanced chemiluminescence detection (Cat. No. WBLUF0100, Sigma-Aldrich, St. Louis, MO, USA). Antibodies: BAX, 1:500 dilution (Clone 2D2, Cat. No. sc-20067, Santa Cruz Biotechnology, Dallas, TX, USA); GAPDH, 1:1000 dilution (Clone 1E6D9, Cat. No. 60004, Proteintech, Rosemont, IL, USA); m-IgGk BP-HRP secondary antibody (Cat. No. sc-516102, Santa Cruz Biotechnology, Dallas, TX, USA).

DATA AND RESOURCE AVAILABILITY

The data supporting the findings of this study are included in this published article (and its supplementary information files). Materials generated in this study are available from the corresponding author upon reasonable request. Structures corresponding to PDB 1F16, 2K7W, and GW60 were used in this study.

1153 **SUPPLEMENTARY INFORMATION**

1154 **Supplementary figure titles:**

1155 Supplementary Figure 1: 2t-hexadecenal promotes BAX functionalization (Related to Figure 1)

1156 Supplementary Figure 2: BAX activation by 2t-hexadecenal does not require cysteine residues
1157 (Related to Figure 2)

1158 Supplementary Figure 3: An assay for detecting BAX early-activation steps reveals that
1159 2t-hexadecenal cooperates with BIM-mediated triggering (Related to Figure 3)

1160 Supplementary Figure 4: Structural, biophysical, and functional approaches identify α8
1161 mobilization as necessary for 2t-hexadecenal function (Related to Figure 4)

1162 Supplementary Figure 5: 1H-15N HSQC perturbations indicate that short-chain 2t-alkenals exhibit
1163 CSPs outside of the BAF region (Related to Figure 5)

1164 Supplementary Figure 6: In silico docking simulations suggest long-chain 2t-alkenals exhibit
1165 increased specificity for the BAF (Related to Figure 5)

1166 Supplementary Figure 7: Long-chain 2t-alkenals are capable of BAX activation (Related to Figure
1167 5)

1168 Supplementary Figure 8: BAF mutations ablate 2t-hexadecenal mediated membrane
1169 permeabilization (Related to Figure 6)

1170 Supplementary Figure 9: Mutating proline 168 disrupts 2t-hexadecenal synergy with BAX and
1171 BIM (Related to Figure 7)

Supplementary Figure Legends

Supplementary Figure 1: 2t-hexadecenal promotes BAX functionalization (Related to Figure 1)

(A–D) LUV permeabilization studies with recombinant BAX protein treated as indicated and measured at regular intervals for changes in fluorescence as fluorophores are released from compromised liposomes. Left panels: kinetic fluorescence data; right panels: endpoint data normalized to LUV fluorescence and maximal signal generated by LUVs solubilized with CHAPS detergent (grey data). Data are shown as the mean of technical replicates and error bars report SEM.
(A) BAX protein (100 nM) was activated by BIM-BH3 peptide (0.13–2 µM) and added to LUVs.
(B) LUVs treated with 2t-16 (16.5–50 µM) in the absence of BAX to confirm no membrane destabilization by 2t-16.
(C) Data summarized by Figure **1F**. LUVs permeabilized by BAX (120 nM) treated with 2t-16 (6.5–50 µM) ± BIM-BH3 peptide (0.5, 2.5 µM).
(D) Data summarized by Figure **1I**. LUVs permeabilized by BAX (160 nM) treated with 16CHO (6.5–50 µM) ± BIM-BH3 peptide (0.5, 2.5 µM).

Supplementary Figure 2: BAX activation by 2t-hexadecenal does not require cysteine residues (Related to Figure 2)

(A) Alexa Fluor 647-labeled recombinant BAX^{WT} (1 nM) was incubated with CHAPS (0.002%) to inhibit oligomerization, treated as indicated, and subjected to MST. Timetrace thermal shift curves of BAX^{WT} titrated with 2t-16 or 16CHO (0.04, 1.25, 40 µM) report the mean of replicate data.
(B–C) The melting temperature of BAX^{WT} and BAX^{2S} ± 2t-16 (6.5−50 µM) was measured by thermal shift assay using SYPRO orange and compared. Statistical significance was determined by two-way ANOVA; ns, not significant ($P > 0.05$).
(D–E) LUV permeabilization studies with recombinant BAX^{2S} protein treated as indicated and measured at regular intervals for changes in fluorescence as fluorophores are released from compromised liposomes. Left panels: kinetic fluorescence data; right panels: endpoint data normalized to LUV fluorescence and maximal signal generated by LUVs solubilized with CHAPS detergent (grey data). Data are shown as the mean of technical replicates and error bars report SEM.
(D) Data summarized by Figure **2F**. LUVs permeabilized by BAX^{2S} (100 nM) treated with 2t-16 (6.5–50 µM) ± BIM-BH3 peptide (0.5, 2.5 µM).
(E) Data summarized by Figure **2I**. LUVs permeabilized by BAX^{2S} (100 nM) treated with 16CHO (6.5–50 µM) ± BIM-BH3 peptide (0.5, 2.5 µM).

Supplementary Figure 3: An assay for detecting BAX early-activation steps reveals that 2t-hexadecenal cooperates with BIM-mediated triggering (Related to Figure 3)

(A) Illustration of BAX and BAK-BH3 interactions within FLAMBE. The reporter is a fluorescently-labeled BAK-BH3 peptide that exhibits changes in Polarization measurements as it is bound by BAX. Over time, the BAX population binds BAK-BH3 peptides resulting in increased Polarization, which eventually plateaus if the entire population forms heterodimers (dotted line). In conditions that activate BAX, activation-induced intramolecular rearrangements within BAX result in the dissociation of the BAK-BH3 peptide and a concomitant decrease in Polarization over time as the population of unbound BAK-BH3 peptide increases (solid line).

33

1215 **(B)** Illustration of FLAMBE data parameterization and analysis. Left: Kinetic Polarization data is
1216 collected for a treatment causing BAX activation and exhibiting accelerated kinetics of BAK^{TAMRA}
1217 dissociation (blue lines, depicted as a titration exhibiting dose-dependent BAX activation). Kinetic
1218 data is parameterized by extracting endpoint Polarization (EP) and time-to-maximum peak (Tmax)
1219 for each condition. Right: Parameterized data are normalized to BAK^{TAMRA} and BAX controls (grey
1220 and black, respectively) and titrations or separate conditions can be visualized as a two-
1221 dimensional plot. Generally, conditions exhibiting minimal or robust activation of the BAX
1222 population cluster in the upper-right or lower-left regions, respectively. Conditions plotted above
1223 BAX (i.e., EP > 1) form stable non-activating complexes with the BAX:BAK^{TAMRA} heterodimer (red
1224 region).
1225 **(C)** BAX^{WT} (60 nM) was treated with BIM-BH3 peptide (0.25–2 µM) and subjected to FLAMBE to
1226 visualize dose-dependent activation-induced dissociation of BAK^{TAMRA}. BIM-BH3 at a low
1227 concentration (0.25 µM, dark blue data) demonstrated a stable, non-activating interaction with the
1228 BAX:BAK^{TAMRA} complex and exhibited increased Polarization.
1229 **(D)** BAX^{WT} (60 nM) was treated with 16CHO (2–50 µM), combined with BAK^{TAMRA} (50 nM), and
1230 subjected to FLAMBE.
1231 **(E)** Same as in **D** with BAX^{2S} (60 nM).
1232 **(F)** Left: BAX^{2S} (60 nM) was treated with three non-activating concentrations of 2t-16 (green: 4.5
1233 µM; orange: 6.5 µM; red: 10 µM). Parameterization of this data is included in **Figure 3D**. Right:
1234 AUC calculated for each condition was normalized to the BAX and BAK^{TAMRA} controls and
1235 reported as a percent change from the vehicle-treated BAX condition.
1236 **(G)** Left: BAX^{WT} (60 nM) was combined with a non-activating concentrations of BIM-BH3 peptide
1237 (0.15 µM) and 2t-16 (4.5 µM), followed by BAK^{TAMRA} (50 nM), and subjected to FLAMBE. Middle:
1238 Parameterized FLAMBE data including three concentrations of 2t-16 (green: 4.5 µM; orange: 6.5
1239 µM; red: 10 µM) in the absence or presence of BIM-BH3 (circle and square datapoints,
1240 respectively). Annotations report the magnitude of shift between data with and without BIM-BH3.
1241 Right: AUC calculated for each condition was normalized to the BAX and BAK^{TAMRA} controls and
1242 reported as a percent change from the vehicle-treated BAX condition.
1243 **(H)** Fluorescence polarization competition assay with recombinant BCL-xL$^{\Delta C}$ protein treated with
1244 2t-16 (2–50 µM) and combined with BAK^{TAMRA}.

1245 **Supplementary Figure 4: Structural, biophysical, and functional approaches identify α8**
1246 **mobilization as necessary for 2t-hexadecenal function (Related to Figure 4)**

1247 **(A)** ^{1}H-^{15}N HSQC NMR spectra of ^{15}N-labeled BAX^{WT} (40 µM) and BAX^{WT} treated with vehicle or
1248 2t-16 (50, 150 µM).
1249 **(B)** Plot of BAX residues exhibiting a significant shift in response to incubation with 2t-16.
1250 **(C)** Chemical shift perturbations (CSPs) observed in ^{15}N-labeled BAX^{WT} incubated with 16CHO
1251 (150 µM). Residues exhibiting a shift greater than 1 or 2 standard deviations above the average
1252 (dotted lines) are highlighted and indicated on the BAX structure (PDB: 1F16). The absence of a
1253 bar indicates no chemical shift difference, the presence of a proline, or the residue that could not
1254 be definitively assigned.
1255 **(D)** Chemical shift perturbations (CSPs) observed in ^{15}N-labeled BAX incubated with 2t-16 (Figure
1256 **4A**) were subtracted by CSPs observed with 16CHO (Figure **S4C**) and plotted as a function of
1257 BAX residues. Residues exhibiting a shift greater than the 1 standard deviation above the average
1258 (dotted line) are colored yellow and indicated on the BAX structure (PDB: 1F16). Residues
1259 uniquely exhibiting significance in the 2t-16 treatment and not 16CHO are highlighted with a black
1260 outline. The absence of a bar indicates no chemical shift difference, the presence of a proline, or
1261 the residue that could not be definitively assigned.

Gelles et al.

1262   **(E)** LUVs permeabilized by reduced BAX$^{\alpha 8}$ (220 nM) treated with BIM-BH3 peptide (0.2–6.5 µM).
1263   Data are shown as the mean of technical replicates and error bars report SEM.
1264   **(F)** Same as in **E** with oxidized BAX$^{\alpha 8}$ (220 nM) to induce a disulfide tether immobilizing α8.
1265   **(G–J)** BAX$^{\alpha 8}$ was treated as indicated, combined with a TAMRA-labeled BAK-BH3 peptide
1266   (BAK^{TAMRA}), and immediately subjected to FLAMBE analysis. Left panels: kinetic Polarization
1267   data; right panels: two-dimensional plot of parameterized FLAMBE data comparing Tmax and
1268   endpoint Polarization metrics normalized to BAK^{TAMRA} (grey data) and the vehicle-treated BAX
1269   control (black data).
1270   **(G)** Reduced BAX$^{\alpha 8}$ (75 nM) was treated with BIM-BH3 (0.06–1 µM), combined with BAK^{TAMRA}
1271   (50 nM), and subjected to FLAMBE.
1272   **(H)** Same as in **G** with oxidized BAX$^{\alpha 8}$ (250 nM) to immobilize α8.
1273   **(I)** Oxidized BAX$^{\alpha 8}$ (250 nM) was treated with 2t-16 (3–50 µM), combined with BAK^{TAMRA} (50 nM),
1274   and subjected to FLAMBE.
1275   **(J)** BAX$^{\alpha 8}$ (225 nM) was treated with four non-activating concentrations of 2t-16 (blue: 3 µM;
1276   green: 4.5 µM; orange: 6.5 µM; red: 10 µM) in the absence or presence of BIM-BH3, followed by
1277   BAK^{TAMRA} (50 nM), and subjected to FLAMBE. Parameterization of this data is included in **Figure**
1278   **4I**.

1279   **Supplementary Figure 5: ^{1}H-^{15}N HSQC perturbations indicate that short-chain 2t-alkenals**
1280   **exhibit CSPs outside of the BAF region (Related to Figure 5)**

1281   **(A)** Chemical shift perturbations (CSPs) observed in ^{15}N-labeled BAX incubated with either 2t-16
1282   (50, 150 µM), 2t-9 (0.3, 0.9, 2.7 mM), or 2t-5 (0.3, 0.9, 2.7 mM) averaged across concentrations.
1283   Residues exhibiting a shift greater than 1 or 2 standard deviations above the average (dotted
1284   lines) are indicated in light and dark colors, respectively, and indicated on the BAX structure (PDB:
1285   1F16). The absence of a bar indicates no chemical shift difference, the presence of a proline, or
1286   the residue that could not be definitively assigned.
1287   **(C–D)** Residues exhibiting significant CSPs for each concentration (0.3, 0.9, 2.7 mM) of 2t-9 or
1288   2t-5. Highlighted residues exhibited shifts greater than 1 standard deviation above the average of
1289   measurable shifts.

1290   **Supplementary Figure 6: In silico docking simulations suggest long-chain 2t-alkenals**
1291   **exhibit increased specificity for the BAF (Related to Figure 5)**

1292   **(A–C)** Unbiased *in silico* rigid docking of 2t-alkenals or S1P against BAX using the SwissDock
1293   web service. Insets display cross-section of ligands docking within the hydrophobic funnel. Models
1294   visualized with PyMOL.
1295   **(A)** Visualization of results for each 2t-alkenal or S1P docking on an unmodified structure of BAX
1296   (PDB: 1F16, BAX^{FL}). Quantification of results summarized in Figure **6C**.
1297   **(B)** As in **A** with ligands docking on a structure of BAX with alpha helix 8 removed (PDB: 1F16,
1298   Δ157–163; BAX$^{\Delta\alpha 8}$). Quantification of results summarized in Figure **6C**.
1299   **(C)** As in **B** with ligands docking on a structure of BAX bound to a BIM-BH3 peptide with alpha
1300   helix 8 removed (PDB: 2K7W, Δ157–163; BAX:BIM).

1301   **Supplementary Figure 7: Long-chain 2t-alkenals are capable of BAX activation (Related to**
1302   **Figure 5)**

1303   **(A)** Alexa Fluor 647-labeled recombinant BAX^{WT} (1 nM) was incubated with CHAPS (0.002%) to
1304   inhibit oligomerization, treated with the indicated 2t-alkenals (0.16–5 µM), and subjected to MST.

1305 Timetrace data are shown as the mean of replicates. Thermophoresis metrics for each 2t-alkenal
1306 are summarized in Figure **5C**.
1307 **(B)** BAX^{2S} (60 nM) was treated with the indicated 2t-alkenal (3–50 µM), combined with BAK^{TAMRA}
1308 (50 nM), and subjected to FLAMBE. Data are shown as the mean of replicates. Parameterized
1309 data reporting EP and Tmax for each experiment are provided in Figures **5D–E**.
1310 **(C)** LUVs permeabilized by BAX^{2S} (100 nM) treated with the indicated 2t-alkenal (6.5–50 µM).
1311 Data are shown as the mean of replicates. Normalized endpoint permeabilization data
1312 summarized in Figure **5F**.

1313 **Supplementary Figure 8: BAF mutations ablate 2t-hexadecenal mediated membrane**
1314 **permeabilization (Related to Figure 6)**

1315 **(A)** Data summarized by Figure **6G**. LUVs permeabilized by WT or BAF mutant BAX activated by
1316 BIM-BH3 (0.125−2 µM).
1317 **(B)** Data summarized by Figure **6H**. LUVs permeabilized by WT or BAF mutant BAX activated by
1318 2t-16 (6.5−50 µM).
1319 **(C)** Data summarized by Figure **6H**. As in **B** with BAX primed with BIM-BH3 peptide (0.15 µM).

1320 **Supplementary Figure 9: Mutating proline 168 disrupts 2t-hexadecenal synergy with BAX**
1321 **and BIM (Related to Figure 7)**

1322 **(A)** Left: BAX^{WT} (60 nM) was combined with a non-activating concentration of BIM-BH3 peptide
1323 (0.15 µM) and 2t-16 (3 µM), followed by BAK^{TAMRA} (50 nM), and subjected to FLAMBE. Right:
1324 Parameterized FLAMBE data in the absence or presence of BIM-BH3 (circle and square
1325 datapoints, respectively). Annotations report the magnitude of shift between data with and without
1326 BIM-BH3. The parameterized trendline for BAX^{WT} is included for comparison in Figure **7D**.
1327 **(B)** Data summarized by Figure **7F**. LUVs permeabilized by WT or P168G BAX activated by
1328 BIM-BH3 (0.125−2 µM).
1329 **(C)** Data summarized by Figure **7G**. LUVs permeabilized by BAX^{P168G} (100 nM) treated with 2t-16
1330 (6.5–50 µM) ± BIM-BH3 peptide (0.5, 2 µM).
1331 **(D)** Western blot confirming expression of BAX protein in transduced *Bax$^{–/–}$Bak$^{–/–}$* MEFs.

REFERENCES

1. Singh, R., Letai, A., and Sarosiek, K. (2019). Regulation of apoptosis in health and disease: the balancing act of BCL-2 family proteins. Nat Rev Mol Cell Biol *20*, 175-193. 10.1038/s41580-018-0089-8.

2. Antonsson, B., Montessuit, S., Lauper, S., Eskes, R., and Martinou, J.C. (2000). Bax oligomerization is required for channel-forming activity in liposomes and to trigger cytochrome c release from mitochondria. Biochem J *345 Pt 2*, 271-278.

3. Kim, H., Tu, H.C., Ren, D., Takeuchi, O., Jeffers, J.R., Zambetti, G.P., Hsieh, J.J., and Cheng, E.H. (2009). Stepwise activation of BAX and BAK by tBID, BIM, and PUMA initiates mitochondrial apoptosis. Mol Cell *36*, 487-499. 10.1016/j.molcel.2009.09.030.

4. Gavathiotis, E., Reyna, D.E., Davis, M.L., Bird, G.H., and Walensky, L.D. (2010). BH3-triggered structural reorganization drives the activation of proapoptotic BAX. Mol Cell *40*, 481-492. 10.1016/j.molcel.2010.10.019.

5. Gahl, R.F., He, Y., Yu, S., and Tjandra, N. (2014). Conformational rearrangements in the pro-apoptotic protein, Bax, as it inserts into mitochondria: a cellular death switch. J Biol Chem *289*, 32871-32882. 10.1074/jbc.M114.593897.

6. Czabotar, P.E., Westphal, D., Dewson, G., Ma, S., Hockings, C., Fairlie, W.D., Lee, E.F., Yao, S., Robin, A.Y., Smith, B.J., et al. (2013). Bax crystal structures reveal how BH3 domains activate Bax and nucleate its oligomerization to induce apoptosis. Cell *152*, 519-531. 10.1016/j.cell.2012.12.031.

7. Bleicken, S., Jeschke, G., Stegmueller, C., Salvador-Gallego, R., Garcia-Saez, A.J., and Bordignon, E. (2014). Structural model of active Bax at the membrane. Mol Cell *56*, 496-505. 10.1016/j.molcel.2014.09.022.

8. Gelles, J.D., Mohammed, J.N., Chen, Y., Sebastian, T.M., and Chipuk, J.E. (2022). A kinetic fluorescence polarization ligand assay for monitoring BAX early activation. Cell Rep Methods *2*. 10.1016/j.crmeth.2022.100174.

9. Kuwana, T., Mackey, M.R., Perkins, G., Ellisman, M.H., Latterich, M., Schneiter, R., Green, D.R., and Newmeyer, D.D. (2002). Bid, Bax, and lipids cooperate to form supramolecular openings in the outer mitochondrial membrane. Cell *111*, 331-342. 10.1016/s0092-8674(02)01036-x.

10. Shamas-Din, A., Bindner, S., Chi, X., Leber, B., Andrews, D.W., and Fradin, C. (2015). Distinct lipid effects on tBid and Bim activation of membrane permeabilization by pro-apoptotic Bax. Biochem J *467*, 495-505. 10.1042/BJ20141291.

11. Vasquez-Montes, V., Rodnin, M.V., Kyrychenko, A., and Ladokhin, A.S. (2021). Lipids modulate the BH3-independent membrane targeting and activation of BAX and Bcl-xL. Proc Natl Acad Sci U S A *118*. 10.1073/pnas.2025834118.

12. Dadsena, S., Cuevas Arenas, R., Vieira, G., Brodesser, S., Melo, M.N., and Garcia-Saez, A.J. (2024). Lipid unsaturation promotes BAX and BAK pore activity during apoptosis. Nat Commun *15*, 4700. 10.1038/s41467-024-49067-6.

13. Chipuk, J.E., Mohammed, J.N., Gelles, J.D., and Chen, Y. (2021). Mechanistic connections between mitochondrial biology and regulated cell death. Dev Cell *56*, 1221-1233. 10.1016/j.devcel.2021.03.033.

14. Tamura, Y., Kawano, S., and Endo, T. (2020). Lipid homeostasis in mitochondria. Biol Chem *401*, 821-833. 10.1515/hsz-2020-0121.

15. Chipuk, J.E., McStay, G.P., Bharti, A., Kuwana, T., Clarke, C.J., Siskind, L.J., Obeid, L.M., and Green, D.R. (2012). Sphingolipid metabolism cooperates with BAK and BAX to promote the mitochondrial pathway of apoptosis. Cell *148*, 988-1000. 10.1016/j.cell.2012.01.038.

16. Nakahara, K., Ohkuni, A., Kitamura, T., Abe, K., Naganuma, T., Ohno, Y., Zoeller, R.A., and Kihara, A. (2012). The Sjogren-Larsson syndrome gene encodes a hexadecenal dehydrogenase of the sphingosine 1-phosphate degradation pathway. Mol Cell *46*, 461-471. 10.1016/j.molcel.2012.04.033.

17. Manzanares-Estreder, S., Pascual-Ahuir, A., and Proft, M. (2017). Stress-Activated Degradation of Sphingolipids Regulates Mitochondrial Function and Cell Death in Yeast. Oxid Med Cell Longev *2017*, 2708345. 10.1155/2017/2708345.

18. Renault, T.T., Floros, K.V., Elkholi, R., Corrigan, K.A., Kushnareva, Y., Wieder, S.Y., Lindtner, C., Serasinghe, M.N., Asciolla, J.J., Buettner, C., et al. (2015). Mitochondrial shape governs BAX-induced membrane permeabilization and apoptosis. Mol Cell *57*, 69-82. 10.1016/j.molcel.2014.10.028.

19. Czabotar, P.E., and Garcia-Saez, A.J. (2023). Mechanisms of BCL-2 family proteins in mitochondrial apoptosis. Nat Rev Mol Cell Biol *24*, 732-748. 10.1038/s41580-023-00629-4.

20. Gelles, J.D., Mohammed, J.N., Santos, L.C., Legarda, D., Ting, A.T., and Chipuk, J.E. (2019). Single-Cell and Population-Level Analyses Using Real-Time Kinetic Labeling Couples Proliferation and Cell Death Mechanisms. Dev Cell *51*, 277-291 e274. 10.1016/j.devcel.2019.08.016.

21. Kumar, A., Byun, H.S., Bittman, R., and Saba, J.D. (2011). The sphingolipid degradation product trans-2-hexadecenal induces cytoskeletal reorganization and apoptosis in a JNK-dependent manner. Cell Signal *23*, 1144-1152. 10.1016/j.cellsig.2011.02.009.

22. Upadhyaya, P., Kumar, A., Byun, H.S., Bittman, R., Saba, J.D., and Hecht, S.S. (2012). The sphingolipid degradation product trans-2-hexadecenal forms adducts with DNA. Biochem Biophys Res Commun *424*, 18-21. 10.1016/j.bbrc.2012.06.012.

23. Cohen, D.T., Wales, T.E., McHenry, M.W., Engen, J.R., and Walensky, L.D. (2020). Site-Dependent Cysteine Lipidation Potentiates the Activation of Proapoptotic BAX. Cell Rep *30*, 3229-3239 e3226. 10.1016/j.celrep.2020.02.057.

24. Sarosiek, K.A., Chi, X., Bachman, J.A., Sims, J.J., Montero, J., Patel, L., Flanagan, A., Andrews, D.W., Sorger, P., and Letai, A. (2013). BID preferentially activates BAK while BIM preferentially activates BAX, affecting chemotherapy response. Mol Cell *51*, 751-765. 10.1016/j.molcel.2013.08.048.

25. Schumacher, F., Neuber, C., Finke, H., Nieschalke, K., Baesler, J., Gulbins, E., and Kleuser, B. (2017). The sphingosine 1-phosphate breakdown product, (2E)-hexadecenal, forms protein adducts and glutathione conjugates in vitro. J Lipid Res *58*, 1648-1660. 10.1194/jlr.M076562.

26. Jarugumilli, G.K., Choi, J.R., Chan, P., Yu, M., Sun, Y., Chen, B., Niu, J., DeRan, M., Zheng, B., Zoeller, R., et al. (2018). Chemical Probe to Identify the Cellular Targets of the Reactive Lipid Metabolite 2- trans-Hexadecenal. ACS Chem Biol *13*, 1130-1136. 10.1021/acschembio.7b01063.

27. Sung, T.C., Li, C.Y., Lai, Y.C., Hung, C.L., Shih, O., Yeh, Y.Q., Jeng, U.S., and Chiang, Y.W. (2015). Solution Structure of Apoptotic BAX Oligomer: Oligomerization Likely Precedes Membrane Insertion. Structure *23*, 1878-1888. 10.1016/j.str.2015.07.013.

28. Jhong, S.R., Li, C.Y., Sung, T.C., Lan, Y.J., Chang, K.J., and Chiang, Y.W. (2016). Evidence for an Induced-Fit Process Underlying the Activation of Apoptotic BAX by an Intrinsically Disordered BimBH3 Peptide. J Phys Chem B *120*, 2751-2760. 10.1021/acs.jpcb.6b00909.

29. Hauseman, Z.J., Harvey, E.P., Newman, C.E., Wales, T.E., Bucci, J.C., Mintseris, J., Schweppe, D.K., David, L., Fan, L., Cohen, D.T., et al. (2020). Homogeneous Oligomers of Pro-apoptotic BAX Reveal Structural Determinants of Mitochondrial Membrane Permeabilization. Mol Cell *79*, 68-83 e67. 10.1016/j.molcel.2020.05.029.

30. Gavathiotis, E., Suzuki, M., Davis, M.L., Pitter, K., Bird, G.H., Katz, S.G., Tu, H.C., Kim, H., Cheng, E.H., Tjandra, N., and Walensky, L.D. (2008). BAX activation is initiated at a novel interaction site. Nature *455*, 1076-1081. 10.1038/nature07396.

31. Leshchiner, E.S., Braun, C.R., Bird, G.H., and Walensky, L.D. (2013). Direct activation of full-length proapoptotic BAK. Proc Natl Acad Sci U S A *110*, E986-995. 10.1073/pnas.1214313110.

32. Reyna, D.E., Garner, T.P., Lopez, A., Kopp, F., Choudhary, G.S., Sridharan, A., Narayanagari, S.R., Mitchell, K., Dong, B., Bartholdy, B.A., et al. (2017). Direct Activation of BAX by BTSA1 Overcomes Apoptosis Resistance in Acute Myeloid Leukemia. Cancer Cell *32*, 490-505 e410. 10.1016/j.ccell.2017.09.001.

33. Pritz, J.R., Wachter, F., Lee, S., Luccarelli, J., Wales, T.E., Cohen, D.T., Coote, P., Heffron, G.J., Engen, J.R., Massefski, W., and Walensky, L.D. (2017). Allosteric sensitization of proapoptotic BAX. Nat Chem Biol *13*, 961-967. 10.1038/nchembio.2433.

34. Garner, T.P., Amgalan, D., Reyna, D.E., Li, S., Kitsis, R.N., and Gavathiotis, E. (2019). Small-molecule allosteric inhibitors of BAX. Nat Chem Biol *15*, 322-330. 10.1038/s41589-018-0223-0.

35. Subburaj, Y., Cosentino, K., Axmann, M., Pedrueza-Villalmanzo, E., Hermann, E., Bleicken, S., Spatz, J., and Garcia-Saez, A.J. (2015). Bax monomers form dimer units in the membrane that further self-assemble into multiple oligomeric species. Nat Commun *6*, 8042. 10.1038/ncomms9042.

36. Bloch, N.B., Wales, T.E., Prew, M.S., Levy, H.R., Engen, J.R., and Walensky, L.D. (2021). The conformational stability of pro-apoptotic BAX is dictated by discrete residues of the protein core. Nat Commun *12*, 4932. 10.1038/s41467-021-25200-7.

37. Robin, A.Y., Iyer, S., Birkinshaw, R.W., Sandow, J., Wardak, A., Luo, C.S., Shi, M., Webb, A.I., Czabotar, P.E., Kluck, R.M., and Colman, P.M. (2018). Ensemble Properties of Bax Determine Its Function. Structure *26*, 1346-1359 e1345. 10.1016/j.str.2018.07.006.

38. Schinzel, A., Kaufmann, T., Schuler, M., Martinalbo, J., Grubb, D., and Borner, C. (2004). Conformational control of Bax localization and apoptotic activity by Pro168. J Cell Biol *164*, 1021-1032. 10.1083/jcb.200309013.

39. Moujalled, D.M., Brown, F.C., Chua, C.C., Dengler, M.A., Pomilio, G., Anstee, N.S., Litalien, V., Thompson, E., Morley, T., MacRaild, S., et al. (2023). Acquired mutations in BAX confer resistance to BH3-mimetic therapy in acute myeloid leukemia. Blood *141*, 634-644. 10.1182/blood.2022016090.

40. Khatun, J., Gelles, J.D., and Chipuk, J.E. (2024). Dynamic death decisions: How mitochondrial dynamics shape cellular commitment to apoptosis and ferroptosis. Dev Cell *59*, 2549-2565. 10.1016/j.devcel.2024.09.004.

41. Hsu, Y.T., and Youle, R.J. (1997). Nonionic detergents induce dimerization among members of the Bcl-2 family. J Biol Chem *272*, 13829-13834. 10.1074/jbc.272.21.13829.

42. McHenry, M.W., Shi, P., Camara, C.M., Cohen, D.T., Rettenmaier, T.J., Adhikary, U., Gygi, M.A., Yang, K., Gygi, S.P., Wales, T.E., et al. (2024). Covalent inhibition of pro-apoptotic BAX. Nat Chem Biol. 10.1038/s41589-023-01537-6.

43. Rizzo, W.B., S'Aulis, D., Dorwart, E., and Bailey, Z. (2022). Sjogren-Larsson syndrome: A biochemical rationale for using aldehyde-reactive therapeutic agents. Mol Genet Metab Rep *30*, 100839. 10.1016/j.ymgmr.2021.100839.

44. Neuber, C., Schumacher, F., Gulbins, E., and Kleuser, B. (2014). Method to simultaneously determine the sphingosine 1-phosphate breakdown product (2E)-hexadecenal and its fatty acid derivatives using isotope-dilution HPLC-electrospray ionization-quadrupole/time-of-flight mass spectrometry. Anal Chem *86*, 9065-9073. 10.1021/ac501677y.
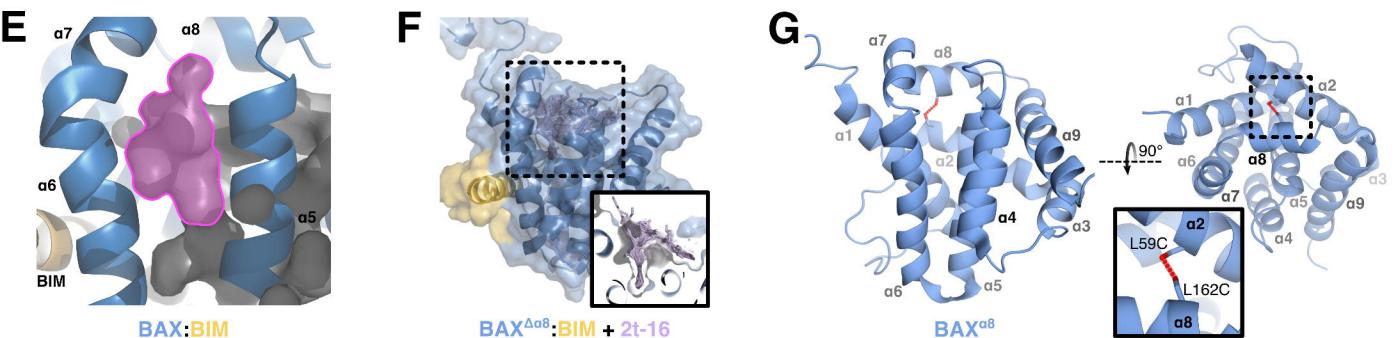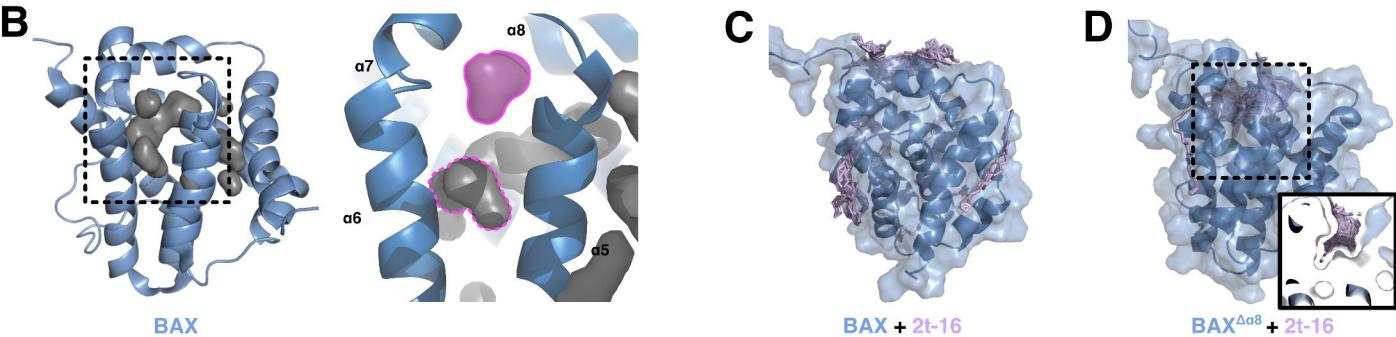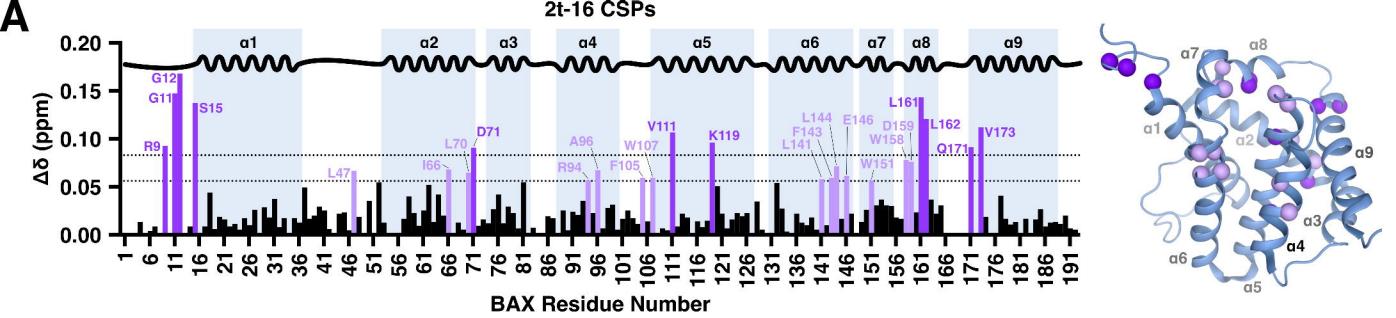
45. Chan, K., Poon, R., and O'Brien, P.J. (2008). Application of structure-activity relationships to investigate the molecular mechanisms of hepatocyte toxicity and electrophilic reactivity of alpha,beta-unsaturated aldehydes. J Appl Toxicol *28*, 1027-1039. 10.1002/jat.1369.

46. LoPachin, R.M., and Gavin, T. (2014). Molecular mechanisms of aldehyde toxicity: a chemical perspective. Chem Res Toxicol *27*, 1081-1091. 10.1021/tx5001046.

47. Edlich, F., Banerjee, S., Suzuki, M., Cleland, M.M., Arnoult, D., Wang, C., Neutzner, A., Tjandra, N., and Youle, R.J. (2011). Bcl-x(L) retrotranslocates Bax from the mitochondria into the cytosol. Cell *145*, 104-116. 10.1016/j.cell.2011.02.034.

48. Todt, F., Cakir, Z., Reichenbach, F., Youle, R.J., and Edlich, F. (2013). The C-terminal helix of Bcl-x(L) mediates Bax retrotranslocation from the mitochondria. Cell Death Differ *20*, 333-342. 10.1038/cdd.2012.131.

49. Suzuki, M., Youle, R.J., and Tjandra, N. (2000). Structure of Bax: coregulation of dimer formation and intracellular localization. Cell *103*, 645-654. 10.1016/s0092-8674(00)00167-7.

50. Dewson, G., Ma, S., Frederick, P., Hockings, C., Tan, I., Kratina, T., and Kluck, R.M. (2012). Bax dimerizes via a symmetric BH3:groove interface during apoptosis. Cell Death Differ *19*, 661-670. 10.1038/cdd.2011.138.

51. Keller, M.A., Zander, U., Fuchs, J.E., Kreutz, C., Watschinger, K., Mueller, T., Golderer, G., Liedl, K.R., Ralser, M., Krautler, B., et al. (2014). A gatekeeper helix determines the substrate specificity of Sjogren-Larsson Syndrome enzyme fatty aldehyde dehydrogenase. Nat Commun *5*, 4439. 10.1038/ncomms5439.

52. Eriksson, A.E., Baase, W.A., Zhang, X.J., Heinz, D.W., Blaber, M., Baldwin, E.P., and Matthews, B.W. (1992). Response of a protein structure to cavity-creating mutations and its relation to the hydrophobic effect. Science *255*, 178-183. 10.1126/science.1553543.

53. Xue, M., Wakamoto, T., Kejlberg, C., Yoshimura, Y., Nielsen, T.A., Risor, M.W., Sanggaard, K.W., Kitahara, R., and Mulder, F.A.A. (2019). How internal cavities destabilize a protein. Proc Natl Acad Sci U S A *116*, 21031-21036. 10.1073/pnas.1911181116.

54. Adamek, D.H., Guerrero, L., Blaber, M., and Caspar, D.L. (2005). Structural and energetic consequences of mutations in a solvated hydrophobic cavity. J Mol Biol *346*, 307-318. 10.1016/j.jmb.2004.11.046.

55. Saito, M., Kono, H., Morii, H., Uedaira, H., Tahirov, T.H., Ogata, K., and Sarai, A. (2000). Cavity-filling mutations enhance protein stability by lowering the free energy of native state. J Phys Chem B *104*, 3705-3711. DOI 10.1021/jp991717f.

56. Robin, A.Y., Krishna Kumar, K., Westphal, D., Wardak, A.Z., Thompson, G.V., Dewson, G., Colman, P.M., and Czabotar, P.E. (2015). Crystal structure of Bax bound to the BH3 peptide of Bim identifies important contacts for interaction. Cell Death Dis *6*, e1809. 10.1038/cddis.2015.141.

57. George, N.M., Evans, J.J., and Luo, X. (2007). A three-helix homo-oligomerization domain containing BH3 and BH1 is responsible for the apoptotic activity of Bax. Genes Dev *21*, 1937-1948. 10.1101/gad.1553607.

58. Liu, X., Dai, S., Zhu, Y., Marrack, P., and Kappler, J.W. (2003). The structure of a Bcl-xL/Bim fragment complex: implications for Bim function. Immunity *19*, 341-352. 10.1016/s1074-7613(03)00234-6.

59. Cowan, A.D., Smith, N.A., Sandow, J.J., Kapp, E.A., Rustam, Y.H., Murphy, J.M., Brouwer, J.M., Bernardini, J.P., Roy, M.J., Wardak, A.Z., et al. (2020). BAK core dimers bind lipids and can be bridged by them. Nat Struct Mol Biol *27*, 1024-1031. 10.1038/s41594-020-0494-5.

60. Miller, M.S., Cowan, A.D., Brouwer, J.M., Smyth, S.T., Peng, L., Wardak, A.Z., Uren, R.T., Luo, C., Roy, M.J., Shah, S., et al. (2024). Sequence differences between BAX and BAK core domains manifest as differences in their interactions with lipids. FEBS J *291*, 2335-2353. 10.1111/febs.17031.
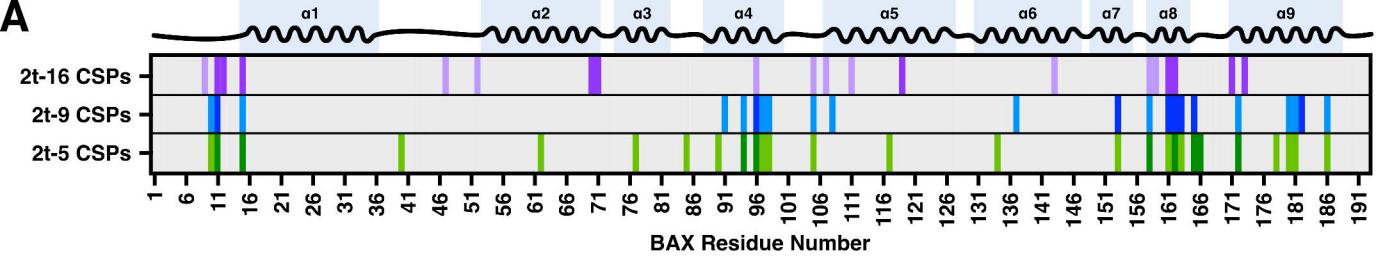
61. Chen, Y., Gelles, J.D., Mohammed, J.N., and Chipuk, J.E. (2023). An optimized protocol for expression and purification of monomeric full-length BAX protein for functional interrogations. Front Cell Dev Biol *11*, 1322816. 10.3389/fcell.2023.1322816.

62. Logue, S.E., Elgendy, M., and Martin, S.J. (2009). Expression, purification and use of recombinant annexin V for the detection of apoptotic cells. Nat Protoc *4*, 1383-1395. 10.1038/nprot.2009.143.

63. Gelles, J.D., and Chipuk, J.E. (2016). Robust high-throughput kinetic analysis of apoptosis with real-time high-content live-cell imaging. Cell Death Dis *7*, e2493. 10.1038/cddis.2016.332.

64. Gelles, J.D., and Chipuk, J.E. (2020). High-Throughput Cell Death Assays with Single-Cell and Population-Level Analyses Using Real-Time Kinetic Labeling (SPARKL). STAR Protoc *1*. 10.1016/j.xpro.2020.100034.

65. Asciolla, J.J., Renault, T.T., and Chipuk, J.E. (2012). Examining BCL-2 family function with large unilamellar vesicles. J Vis Exp. 10.3791/4291.

66. Kong, A.T., Leprevost, F.V., Avtonomov, D.M., Mellacheruvu, D., and Nesvizhskii, A.I. (2017). MSFragger: ultrafast and comprehensive peptide identification in mass spectrometry–based proteomics. Nature methods *14*, 513-520.

67. Geiszler, D.J., Kong, A.T., Avtonomov, D.M., Yu, F., da Veiga Leprevost, F., and Nesvizhskii, A.I. (2021). PTM-Shepherd: analysis and summarization of post-translational and chemical modifications from open search results. Molecular & Cellular Proteomics *20*.

68. Yu, F., Haynes, S.E., and Nesvizhskii, A.I. (2021). IonQuant enables accurate and sensitive label-free quantification with FDR-controlled match-between-runs. Molecular & Cellular Proteomics *20*.

69. Li, K., Vaudel, M., Zhang, B., Ren, Y., and Wen, B. (2019). PDV: an integrative proteomics data viewer. Bioinformatics *35*, 1249-1251. 10.1093/bioinformatics/bty770.

70. Mohammed, J.N., Gelles, J.D., and Chipuk, J.E. (2022). FLAMBE: A kinetic fluorescence polarization assay to study activation of monomeric BAX. STAR Protoc *3*, 101252. 10.1016/j.xpro.2022.101252.

71. Zhang, H., Nimmer, P., Rosenberg, S.H., Ng, S.C., and Joseph, M. (2002). Development of a high-throughput fluorescence polarization assay for Bcl-x(L). Anal Biochem *307*, 70-75. 10.1016/s0003-2697(02)00028-3.

72. Masse, J.E., and Keller, R. (2005). AutoLink: automated sequential resonance assignment of biopolymers from NMR data by relative-hypothesis-prioritization-based simulated logic. J Magn Reson *174*, 133-151. 10.1016/j.jmr.2005.01.017.

73. Grosdidier, A., Zoete, V., and Michielin, O. (2011). Fast docking using the CHARMM force field with EADock DSS. J Comput Chem *32*, 2149-2159. 10.1002/jcc.21797.

74. Grosdidier, A., Zoete, V., and Michielin, O. (2011). SwissDock, a protein-small molecule docking web service based on EADock DSS. Nucleic Acids Res *39*, W270-277. 10.1093/nar/gkr366.

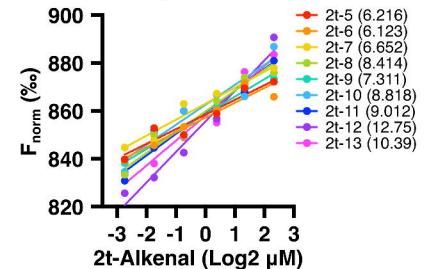**A** WT MEFs — left: Time course (0–24 hours), # AV+ (×1000), conditions Ctrl, ABT, 2t-16 gradient; right: bar graph Ctrl (black), ABT (red), 2t-16 gradient.

B *Bim⁻/⁻ Bid⁻/⁻* MEFs — left: Time course (0–24 hours), # AV+ (×1000), Ctrl, ABT, 2t-16 gradient; right: bar graph Ctrl (yellow), ABT (red), 2t-16 gradient.

C *Bax⁻/⁻ Bak⁻/⁻* MEFs — left: Time course (0–24 hours), # AV+ (×1000), Ctrl, ABT, 2t-16 gradient; right: bar graph Ctrl (blue), ABT (red), 2t-16 gradient.

D BAX — RFU (×1000) vs Time (minutes), 2t-16 gradient, Ctrl, CHAPS.

E BAX+BIM — RFU (×1000) vs Time (minutes), 2t-16 gradient, Ctrl, CHAPS.

F % LUV Permeabilization, 2t-16

BAX	3	10	13	18	29	35	49
	6	13	19	29	37	49	54
BIM	34	49	55	62	73	86	88

G BAX — RFU (×1000) vs Time (minutes), 16CHO gradient, Ctrl, CHAPS.

H BAX+BIM — RFU (×1000) vs Time (minutes), 16CHO gradient, Ctrl, CHAPS.

I % LUV Permeabilization, 16CHO

BAX	2	1	1	1	3	3	0
	19	18	12	17	16	18	19
BIM	30	30	26	29	28	28	29

A

Thermophoresis + T-Jump

K_D: 0.182 μM

B Timetrace Curve Fit

C

	Peptide Fragment	Residues	Cys	BAX	BAX+2t-16
1	ALC[+57.0215]TKVPELIR	124–134	C126	3.10E8	4.35E8
2	M[+15.9949]GGEAPELALDPVPQDASTKKLSEC[+57.0215]LK	38–64	C62	1.00E8	9.85E7
3	MGGEAPELALDPVPQDASTKKLSEC[+57.0215]LK	38–64	C62	5.16E9	4.82E9
4	LSEC[+57.0215]LKRIGDELDSNMELQR	59–78	C62	4.42E8	4.28E8

D BAX²ˢ

E BAX²ˢ+BIM

F % LUV Permeabilization

G BAX²ˢ

H BAX²ˢ+BIM

I % LUV Permeabilization

A **BAX^WT**

B **BAX^2S**

C "Primed" BAX^2S

D "Triggered" BAX^2S

E

F

G

A 2t-16 CSPs

α1, α2, α3, α4, α5, α6, α7, α8, α9

BAX Residue Number

Δδ (ppm)

Labels: G12, G11, S15, R9, L47, L70, I66, R94, D71, A96, F105, W107, F105, V111, K119, L144, F143, L141, E146, D159, W151, W158, L161, L162, Q171, V173

B BAX

α8, α7, α6, α5

C BAX + 2t-16

D BAX^Δα8 + 2t-16

E BAX:BIM

α7, α8, α6, α5, BIM

F BAX^Δα8:BIM + 2t-16

G BAX^α8

α7, α8, α1, α2, α6, α5, α4, α3, α9

L59C, L162C, α2, α8

H S75 10/300

158 kD, 44 kD, 14 kD

20 21 22 23 24 25 26 27 28 29 30 31 32 33 34 35 36

BAX^α8, 2t-16, BIM

BAX^α8-AF488

I "Primed" BAX^α8

Polarization (mP)

Time (minutes)

BAK^TAMRA, BAX^α8, BIM, 2t-16

0.412, 0.430, 0.541, 0.509, 0.418

Norm Endpoint

Norm Tmax

A Hydrophobic (green), Polar (cyan), Selected (yellow)

Residues shown: L59, I152, L144, F143, L148, T140, A117, F114, L113, F92, L27, L26, W107, V110, L63, L62, C62

α2 (blue), α5 (purple), α6 (magenta)

B BAX$^{\Delta\alpha8}$:BIM + 2t-16

C V110L, L113M, L144F

D

	WT	V110L	L113M	L144F
Number of poses	9	10	10	10
Top Glide score	-4.481	-3.407	-2.736	-3.256
Avg Glide score	-4.074	-2.777	-2.437	-2.570
Top Emodel score	-29.68	-25.52	-25.31	-24.92

E BAX$^{V110L\Delta\alpha8}$:BIM + 2t-16   BAX$^{L113M\Delta\alpha8}$:BIM + 2t-16   BAX$^{L144F\Delta\alpha8}$:BIM + 2t-16

F T_m (°C)

WT ~74, V110L ~70.5, L113M ~69, L144F ~69.5 (*** significance)

G % LUV Permeabilization

WT	3	10	20	30	45	52
V110L	5	22	35	45	50	58
L113M	1	2	5	26	37	47
L144F	4	19	30	43	57	62

BIM

H % LUV Permeabilization

−BIM

WT	8	20	26	34	44	61	62
V110L	6	7	8	8	9	10	9
L113M	7	7	8	8	9	10	9
L144F	7	6	6	5	6	8	11

2t-16

+BIM

WT	15	31	39	47	56	63	66
V110L	15	14	15	13	11	12	10
L113M	18	18	20	19	25	32	33
L144F	18	17	12	13	16	19	17

2t-16

A
α7
P168G BAF
WT BAF
α2
BAX$^{P168G\Delta\alpha8}$ + 2t-16
α6 α5 α9

B
Hydrophobic
Polar
Glycine
α1
α2
α5

V 177
V 173
W 107
G 108
L 59
I 66
I 19
L 144
V 110
L 63
V 111
T 22
G 23
F 114
L 26
I 152

C
P168G 2t-16
WT 2t-16
Interaction Residues
WT
no interaction
P168G
BAX$^{\Delta\alpha8}$:BIM

D
"Primed" BAX^{P168G}
Polarization (mP)
Time (minutes)
BAK^{7AMRA}
BAX^{P168G}
BIM
2t-16
Norm Endpoint
Norm Tmax
0.418
0.658
0.578
0.080
0.045

E
T$_m$ (°C)
WT
P168G
***
ΔT$_m$ (°C)
BAX^{WT}
BAX^{P168G}
2t-16
***

F
% LUV Permeabilization
WT
P168G
0
BIM
1 2 5 19 37 44
0 1 1 3 18 33

G
% LUV Permeabilization
P168G
BIM
0
2t-16
0 0 1 1 1 2 2
6 2 3 3 3 3 8
20 16 16 16 18 26 30

H
Bax$^{-/-}$Bak$^{-/-}$ MEFs + BAX^{WT}
Bax$^{-/-}$Bak$^{-/-}$ MEFs + BAX^{P168G}
AV+ (×100)
Time (hours)
Ctrl
ABT
2t-16

I
AV+ (×100)
Bax$^{-/-}$Bak$^{-/-}$ MEFs
+ BAX^{WT}
+ BAX^{P168G}
ABT-737:
2t-16

J
α1
α8
α9
α6 α5 α2
BAX
BIM
2t-16
MOMP

A FLAMBE Polarization Timetrace

BAX protein + Labeled BAK peptide

Maximum BAX:BAK heterodimerization (no BAX activation)

BAK binding

BAX activation

BAK peptide dissociation

Loss of BAX:BAK heterodimers

Population Status

BAK peptide | BAX protein

Activated BAX

Polarization

B Kinetic Data Parameterization

Treatment Titration

BAX

BAK^TAMRA

Data Summary & Trend Overview

Normalized Endpoint

Normalized Tmax

BAX activation

C BAX^WT

BIM

Ctrl

BAK^TAMRA

Norm Endpoint

Norm Tmax

D BAX^WT

16CHO

Ctrl

BAK^TAMRA

Norm Endpoint

Norm Tmax

E BAX^2S

16CHO

Ctrl

BAK^TAMRA

Norm Endpoint

Norm Tmax

F BAX^2S+2t-16

2t-16

BAK^TAMRA

%Δ Norm AUC

BIM   2t-16   2t-16

G "Primed" BAX^WT

BAK^TAMRA
BAX^WT
BIM
2t-16

0.588
1.096
1.174
0.998

Norm Endpoint

Norm Tmax

%Δ Norm AUC

BIM   2t-16   2t-16

H BCL-xL^ΔC

2t-16

Ctrl

BAK^TAMRA

A

Avg 2t-16 CSPs

Avg 2t-9 CSPs

Avg 2t-5 CSPs

BAX Residue Number

B

BAX Residue Number

C

BAX Residue Number

A BAX^FL

2t-5　2t-6　2t-7　2t-8　2t-9　2t-10

2t-11　2t-12　2t-13　2t-14　2t-15　S1P

B BAX^Δα8

2t-5　2t-6　2t-7　2t-8　2t-9　2t-10

2t-11　2t-12　2t-13　2t-14　2t-15　S1P

C BAX:BIM

2t-5　2t-6　2t-7　2t-8　2t-9　2t-10

2t-11　2t-12　2t-13　2t-14　2t-15　S1P

A "Primed" BAX^WT

B BAX^WT, BAX^P168G

C BAX^P168G, BAX^P168G+BIM [low], BAX^P168G+BIM [high]

D Bax^−/−Bak^−/− MEFs